Reluctance-Based Dynamic Models for Multiphase Coupled Inductor Buck Converters

Daniel H. Zhou, Student Member, IEEE, Youssef Elasser, Student Member, IEEE, Jaeil Baek, Member, IEEE, and Minjie Chen, Senior Member, IEEE

Abstract—This paper investigates reluctance-based dynamic models for multiphase coupled inductor buck converters. A reluctance-based state-space model is derived based on the inductance dual model of the coupled inductor. The physical core geometry is explicitly related to the circuit's dynamic properties to provide useful insights for coupled inductor design, especially if the number of phases is large. The transfer functions of multiphase coupled inductor buck converters with an arbitrary number of phases are derived based on the inductance dual model. It is shown that a symmetric multiphase coupled inductor buck converter can be modeled as a second-order dynamic system when perturbed with a common-mode duty cycle change, and the duty cycle to output voltage and output current transfer functions are determined by the leakage flux path of the coupled inductor. The differential-mode current balancing mechanisms of the multiphase coupled inductor buck converter are decoupled from other system dynamics and are determined only by the winding resistance and magnetizing flux path. The applicability of the model in cases with structural asymmetry are discussed, with the results supporting the feasibility of scaling the coupled inductor structure to a large number of phases with tolerance for asymmetry. The dynamic models are verified by SPICE simulations and experimental results.

Index Terms—coupled inductor, multiphase buck converter, modeling and control, interphase transformer, inductance dual model, current balancing, state-space model, transfer function.

I. INTRODUCTION

fundamental trade-off in the design of point-of-load converters is sizing the inductive elements to balance steady state and transient performance [1]–[4]. A smaller inductance is important to improve converter bandwidth and ensure the output stays in regulation during load transients. However, a larger inductance is also desired to reduce steady state current ripple; reduced current ripple improves converter efficiency, eases maximum current stress, reduces the required output capacitor size, and relaxes saturation flux requirements on the magnetic core.

One method of addressing this trade-off is the use of multiphase converters with coupled inductors. The frequency of the output current ripple is multiplied and the ripple amplitude is reduced by interleaving multiple parallel phases with a coupled inductor [5]–[12]. The use of coupled inductors is also attractive since they have reduced energy storage requirements,

This paper was presented at the 2020 IEEE 21st Workshop on Control and Modeling for Power Electronics (COMPEL) [1].

The authors are with the Department of Electrical Engineering and Andlinger Center for Energy and the Environment at Princeton University, Princeton, NJ, 08540, USA.

This work was supported in part by NSF CAREER Award No. 1847365, and in part by the Princeton SEAS Innovation Fund.

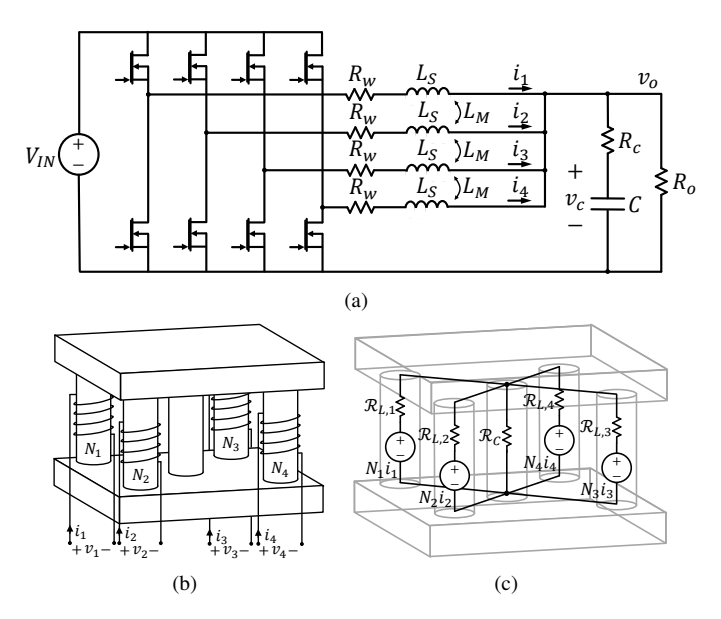


Fig. 1. (a) Schematic of a buck converter with a four-phase coupled inductor, (b) drawing of a four-phase coupled inductor, and (c) reluctance model of a four-phase coupled inductor.

allowing them to achieve similar transient and steady state performance in less space than multiple discrete inductors [13]–[17]. Designers can balance the efficiency, power density, and transient performance across a wide range of operating conditions by optimizing the magnetic structure and winding geometry. Coupled inductors have numerous degrees of design freedom and complex magnetic behaviors. This makes the design and optimization of high performance coupled inductors challenging, especially at high switching frequencies.

A coupled inductor can be equivalently modeled by its self and mutual inductances, magnetizing and leakage inductances, or magnetic reluctances [1], [3]–[5]. These methods all describe the same mathematical relationships between coupled inductor windings, making them functionally identical and freely interchangeable. However, as presented in [3], the inductance dual model is especially suitable for dynamic analysis and informing physical core design.

Understanding the dynamic characteristics of point-of-load converters is important for designing coupled inductors with good transient performance. The dynamic models of many single-phase and multiphase converters with coupled and uncoupled inductors have been studied, including boost, buck, and other PWM converters [18]–[26]. An additional concern in multiphase converter design is current balancing. Ideally,

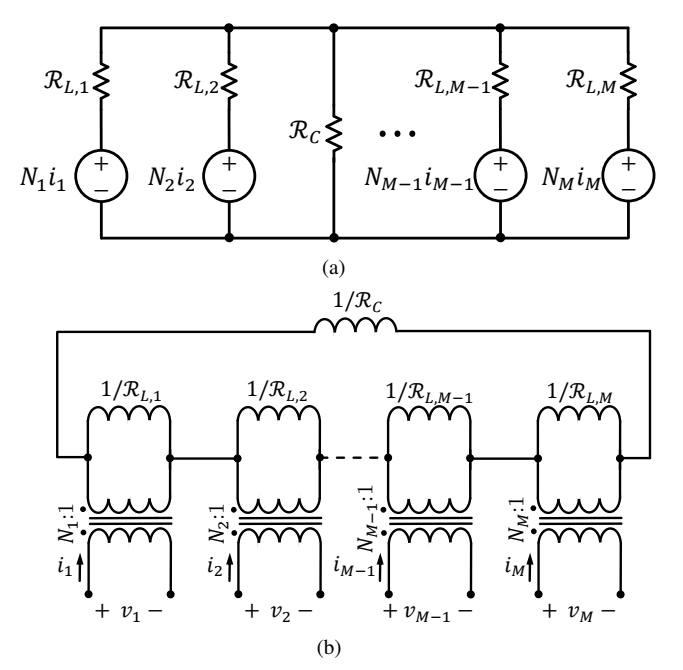


Fig. 2. (a) Reluctance model and (b) inductance dual model describing the coupled inductor in terms of side leg reluctances $\mathcal{R}_{L1} \dots \mathcal{R}_{LM}$ and the center leg reluctance \mathcal{R}_C . The models are mathematically identical topological duals [43]–[45]; one model describes the coupled inductor in the magnetic domain and the other describes it in the circuit domain.

current should be equally shared between every phase to minimize losses, reduce peak current stress, and prevent core saturation [27]-[29]. Non-idealities in hardware and control may cause large current imbalances [12] which must be corrected with active current balancing. Typically, this problem is approached by separating the total current control from the first-order differential current control [30]–[42]. In particular, [33] suggests a state transformation where the differences between individual phase currents and the average are controlled, a technique which is rigorously shown to decouple the current balancing and output voltage control problems. Studies on dynamic models for two-phase coupled inductor buck converters based on the inductance matrix exist [5]. However, elements of the inductance matrix are not explicit design parameters and cannot be easily determined before the magnetic structure is designed or fabricated. Experimental measurements or finiteelement-modeling (FEM) are needed to identify elements of the inductance matrix. As a result, these dynamic models provide limited guidance for practical design and they have not been extended to cover cases with an arbitrary number of phases or sophisticated magnetic structures.

This paper, for the first time, explicitly presents dynamic models of the coupled inductor buck converter with an arbitrary number of phases. This is enabled by using the inductance dual model. The inductance dual model [3], [4] elucidates the magnetic flux flow in each phase of the coupled inductor, which helps relate the physical core design to the converter's dynamic performance. The inductance dual model also reveals the key flux paths that dictate the converter's dynamic behavior. The models derived in this paper show that the symmetric multiphase coupled inductor buck converter can be modeled as a second-order dynamic system for common-

mode duty cycle perturbations. The dynamic models also show that the duty cycle to output voltage and output current transfer functions are entirely determined by the leakage flux path of the coupled inductor. The current balancing dynamics of the multiphase coupled inductor buck converter are decoupled from other system dynamics and are determined only by the magnetizing flux path of the coupled inductor. These key findings are verified using SPICE simulations and experimental results. Design guidelines to improve the dynamic performance of coupled inductors are provided.

The remainder of this paper is arranged as follows: Section II reviews the inductance dual model of the coupled inductor and compares it to the self and mutual inductance model. Section III derives a state-space model of the multiphase coupled inductor buck converter and reduces it to several simpler forms for controlling the output voltage, total current, and differential currents. Section IV introduces the experimental setup. Section V verifies the theoretical predictions using SPICE simulations and experimental results. Section VI discusses the applicability and limitations of the dynamic models in cases with structural asymmetry. Finally, we summarize our main conclusions in section VII.

II. MAGNETIC MODELS FOR THE COUPLED INDUCTOR

Figure 1a shows the schematic of a four-phase coupled inductor buck converter. The coupled inductor structure shown in Fig. 1b is selected to demonstrate the principles of coupled inductor dynamics. There is one coil coupled to each of the four side legs and a shared center leg carrying the returning flux. The legs are connected by a top and bottom plate with low reluctance. A coupled inductor with this structure and Mphases may be modeled with the reluctance model in Fig. 2a. In this model, the center leg is represented with a reluctance \mathcal{R}_C and the side legs have reluctances $\mathcal{R}_{L,1}, \mathcal{R}_{L,2}, \dots, \mathcal{R}_{L,M}$. A magneto-motive-force (MMF) source represents each coil connection, with N_1, N_2, \ldots, N_M turns per phase. If the center leg reluctance is much larger than the side leg reluctances, most of the flux generated by one of the coils will travel through the other legs (magnetizing flux) instead of the center leg (leakage flux).

This reluctance model assumes that the top and bottom plates have negligible reluctances, that is, plates having large thickness or high permeability. Because the plate reluctances are negligible, the reluctance paths between all the legs are effectively shorted, regardless of the leg positions. Moreover, the center leg can be repositioned around the plates without introducing asymmetry or changing the schematic in Fig. 2a. The leakage reluctance paths outside of the magnetic core can be lumped together with the center leg reluctance. The center leg may even be removed, and the \Re_C term can represent the distributed reluctance of air between the plates that leakage flux can travel through. So, if the plate reluctances are negligible, we may abstract the physical center leg to a generalized flux path between the plates shared by all phases.

An equivalent model of the coupled inductor is the inductance dual model in Fig. 2b. The inductance dual model is the topological dual of the reluctance model and is functionally identical [3], [4], [43]–[45]. This model is used

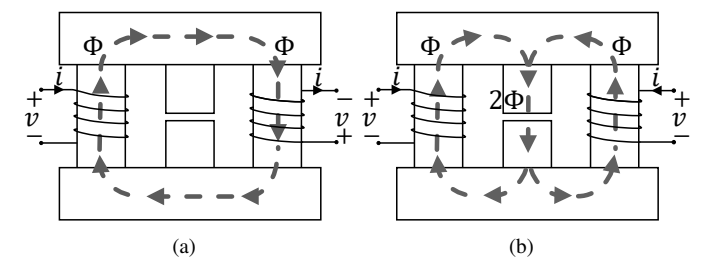


Fig. 3. (a) Magnetizing flux flow through the side legs with no flux in the center leg when two windings are perturbed differentially. (b) Leakage flux flow when two windings are perturbed identically and the flux flows through the center leg. If the center leg reluctance is high, the windings see a higher inductance in differential-mode and a lower inductance in common-mode.

to derive the dynamic equations of the multiphase coupled inductor buck converter. As we will show, this approach greatly simplifies the analysis and highlights important dynamic properties of the circuit. Generally, the coupled inductor may have a different number of turns and different side leg reluctances for each phase. We first assume a symmetric coupled inductor structure with the same number of turns $N_1 = N_2 = \cdots = N_M = N$ and the same side leg reluctance $\mathcal{R}_{L,1} = \mathcal{R}_{L,2} = \cdots = \mathcal{R}_{L,M} = \mathcal{R}_L$ for every phase, then discuss the applicability and limitations of the model in asymmetric cases. The insights and conclusions revealed by this paper are applicable to general coupled inductor structures with sophisticated coupling configurations.

The currents and voltages as labeled in the inductance dual model in Fig. 2b are related by a reluctance matrix:

$$N^{2} \begin{bmatrix} \frac{di_{1}}{dt} \\ \frac{di_{2}}{dt} \\ \vdots \\ \frac{di_{M}}{dt} \end{bmatrix} = \begin{bmatrix} \mathcal{R}_{L} + \mathcal{R}_{C} & \mathcal{R}_{C} & \cdots & \mathcal{R}_{C} \\ \mathcal{R}_{C} & \mathcal{R}_{L} + \mathcal{R}_{C} & \cdots & \mathcal{R}_{C} \\ \vdots & \vdots & \ddots & \vdots \\ \mathcal{R}_{C} & \mathcal{R}_{C} & \cdots & \mathcal{R}_{L} + \mathcal{R}_{C} \end{bmatrix} \begin{bmatrix} v_{1} \\ v_{2} \\ \vdots \\ v_{M} \end{bmatrix}.$$

$$(1)$$

Alternatively, the coupled inductor may be parameterized in terms of its magnetizing inductance L_{μ} and leakage inductance L_{l} . L_{μ} and L_{l} are derived in Appendix I and are defined analogously to a multiwinding transformer model [3]. In brief, the magnetizing inductance L_{μ} describes the flux generated by one phase that flows through the other legs:

$$L_{\mu} = \frac{N^2(M-1)\mathcal{R}_C}{\mathcal{R}_L(M\mathcal{R}_C + \mathcal{R}_L)}.$$
 (2)

The magnetizing inductance is important to differential-mode current balancing. When an equal and opposite current is generated in two different phases, the differential flux only travels through the two side legs and not the center leg, as shown in Fig. 3a. For tightly coupled inductors with multiple phases, the magnetizing inductance determines the dynamics associated with differential current balancing. Therefore, differential current balancing can be sped up by decreasing the magnetizing inductance, which can be done by increasing \mathcal{R}_L .

The flux that flows through the center leg is the leakage flux and is described by the leakage inductance:

$$L_l = \frac{N^2}{M\mathcal{R}_C + \mathcal{R}_L}. (3)$$

TABLE I
KEY DESIGN PARAMETERS DESCRIBED BY RELUCTANCE PARAMETERS
AND INDUCTANCE PARAMETERS

Design Target	by Reluctance Parameters	by Inductance Parameters [3]	
Center Leg Reluctance	\mathcal{R}_C	$\frac{-N^2 L_M}{(L_S - L_M)(L_S + (M-1)L_M)}$	
Side Leg Reluctance	\mathcal{R}_L	$rac{N^2}{L_S - L_M}$	
Common-Mode Dynamics	$\frac{N^2}{M\mathcal{R}_C + \mathcal{R}_L} \approx \frac{N^2}{M\mathcal{R}_C}$	$L_S + L_M(M-1)$	
Differential-Mode Dynamics	$rac{N^2}{\Re_L}$	$L_S - L_M$	

While \Re_C , \Re_L , M and N are explicit design parameters, L_M and L_S can only be obtained by experimental measurements or finite-element modeling.

TABLE II Transfer Functions Derived Based on Reluctance Parameters

Transfer Function by Reluctance Parameters		
*2-phase $\frac{\tilde{v_o}}{\tilde{d}}$	$\frac{2V_{IN}R_o}{CL_lR_os^2 + L_ls + 2R_o} \ [25]$	
$^{\dagger}M$ -phase $\frac{\tilde{v_o}}{\tilde{d}}$	$\frac{MV_{IN}R_o}{CL_lR_os^2 + L_ls + MR_o}$	
$^{\dagger}M$ -phase $\frac{\Delta \tilde{i}}{\Delta \tilde{d}}$	$rac{V_{IN}\mathcal{R}_L}{sN^2}$	

Simplified by assuming $R_w=0$ and $R_c=0$. * The equation derived in [25] is reorganized in terms of L_l .

TABLE III Transfer Functions Derived Based on Inductance Parameters

Transfer Function by Inductance Parameters		
$^\ddagger 2$ -phase $\frac{\tilde{v_o}}{\tilde{d}}$	$\frac{2V_{IN}R_o}{CR_o(L_S+L_M)s^2+(L_S+L_M)s+2R_o}$	
$^{\ddagger}M$ -phase $\frac{\tilde{v_o}}{\tilde{d}}$	$\frac{MV_{IN}R_{o}}{CR_{o}(L_{S}+L_{M}(M-1))s^{2}+(L_{S}+L_{M}(M-1))s+MR_{o}}$	
\S{M} -phase $\frac{\Delta \tilde{i}}{\Delta \tilde{d}}$	$\frac{V_{IN}}{s(L_S - L_M)}$ [34]	

Simplified by assuming $R_w = 0$ and $R_c = 0$.

[‡] Contribution of this work.

The leakage inductance is important to the common-mode dynamic properties of the multiphase coupled inductor buck converter. When the currents in all phases are increased or decreased together, every side leg generates the same flux and it must all pass through the center leg, as shown in Fig. 3b. Therefore, the common-mode dynamics associated with changing all the phase currents together depends on the leakage inductance L_l . It follows that one can improve the system bandwidth by decreasing the leakage inductance, which can be achieved by increasing the number of phases M or maximizing \Re_C .

Modeling the coupled inductor in terms of reluctances \mathcal{R}_L and \mathcal{R}_C is mathematically equivalent to modeling it in terms of self and mutual inductances L_S and L_M ; the dynamic equations are described either in terms of a reluctance matrix or its inverse, a self and mutual inductance matrix. Although these methods are functionally identical, the reluctance-based approach presented in this paper enables the explicit derivation of the dynamic models for an arbitrary number of phases,

[§]The equation derived in [34] is reorganized in terms of L_S and L_M .

which are not found in previous literature. As summarized in Table I, the reluctance-based approach relates the coupled inductor design to the dynamic behavior of the converter more clearly than the inductance matrix approach. Furthermore, the reluctance-based transfer functions depend on fewer physical design parameters. Table II and Table III compare transfer functions written with reluctance parameters and inductance parameters; two transfer functions are presented in previous literature and four transfer functions are contributions of this work. A complete list of the transfer functions derived in this work are included in Tables IV and V.

III. DYNAMIC MODELS FOR THE MULTIPHASE COUPLED INDUCTOR BUCK CONVERTER

In this section, we derive dynamic models of the coupled inductor buck converter with M phases. We assume the converter has a load resistor R_o , a capacitor series resistance R_c , a lumped winding resistance R_w for each phase, and a constant input voltage V_{IN} . The winding resistance R_w includes trace and wire resistance between the switch node and the output voltage node.

Figure 4 shows the switching waveforms of a four-phase coupled inductor buck converter where the switching and phase currents are interleaved. If the phases of an M-phase converter are numbered as k = 1, 2, ..., M, phase k is connected to V_{IN} starting at time $\frac{(k-1)T}{M}$. For the four-phase example, one phase turns on at the time instances $t=0,\frac{T}{4},\frac{T}{2},$ and $\frac{3T}{4}$. Phase k remains connected to V_{IN} for a duration d_kT , where $0 < d_k < 1$ is the duty cycle of that phase.

A. Modeling the M-phase Coupled Inductor Buck Converter

The system shown in Fig 1a contains one capacitor and Minductors, so there are M+1 state variables. We select the state vector $\mathbf{x} = \begin{bmatrix} i_1, i_2, \dots, i_M, v_c \end{bmatrix}^T$. The capacitor voltage v_c is chosen as one of the states instead of the output voltage v_o to simplify the design equations. Each phase has an independent duty cycle and so we select the input vector $\mathbf{u} = \begin{bmatrix} d_1, d_2, \dots, d_M \end{bmatrix}^T$. The output vector is chosen as $\mathbf{y} = \begin{bmatrix} i_1, i_2, \dots, i_M, v_o \end{bmatrix}^T$, which includes the output voltage v_o . We seek a state-space model of the M-phase converter with state matrix A, input matrix B, and output matrix E:

$$\dot{\mathbf{x}} = \mathbf{A}\mathbf{x} + \mathbf{B}\mathbf{u},\tag{4}$$

$$y = Ex, (5)$$

where the output matrix is denoted E rather than the commonly used C to avoid confusion with the output capacitance. The M+1 by M+1 matrix A, derived in Appendix II, is

$$\mathbf{A} = \begin{bmatrix} \alpha & \beta & \cdots & \beta & \beta & \gamma \\ \beta & \alpha & \cdots & \beta & \beta & \gamma \\ \vdots & \vdots & \ddots & \vdots & \vdots & \vdots \\ \beta & \beta & \cdots & \alpha & \beta & \gamma \\ -\frac{\beta}{\delta} - \frac{\beta}{\delta} - \cdots & \frac{\beta}{\delta} - \frac{\alpha}{\delta} & \gamma & \frac{\gamma}{\rho} - \end{bmatrix},$$
(6)

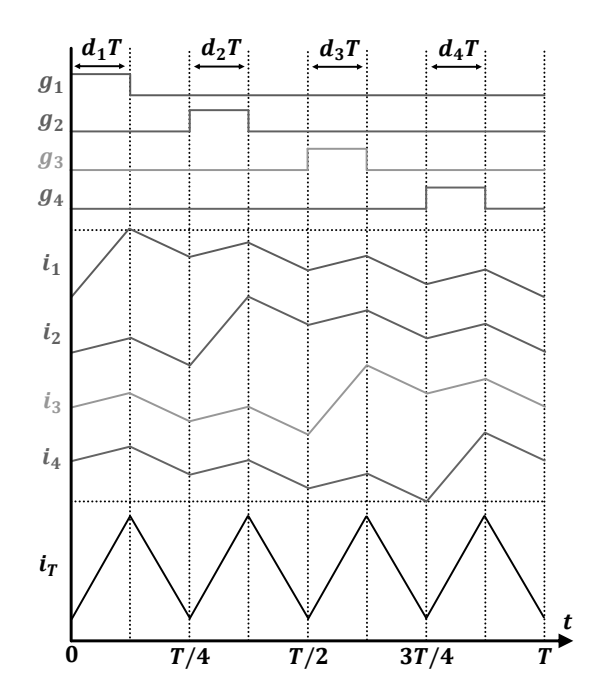


Fig. 4. Switching waveforms and phase currents of a four-phase coupled inductor buck converter. The four phases are interleaved and the gate signals g_1, g_2, g_3, g_4 are equally spaced in the period T. The ripple frequency of the total current i_T is multiplied by four due to interleaving.

with the constants

$$\alpha = \frac{-R_w(\Re_L + \Re_C) - (R_c||R_o)(M\Re_C + \Re_L)}{N^2}, \quad (7)$$

$$\beta = \frac{-\Re_C R_w - (R_c||R_o)(M\Re_C + \Re_L)}{N^2}, \quad (8)$$

$$\beta = \frac{-\Re_C R_w - (R_c||R_o)(M\Re_C + \Re_L)}{N^2},$$
 (8)

$$\gamma = \frac{-(M\mathcal{R}_C + \mathcal{R}_L)R_o}{N^2(R_c + R_o)},$$

$$\delta = \frac{R_o}{C(R_o + R_c)},$$
(10)

$$\delta = \frac{R_o}{C(R_o + R_c)},\tag{10}$$

$$\rho = -\frac{1}{C(R_o + R_c)},\tag{11}$$

where $(R_c||R_o)$ is the parallel combination of the capacitor series resistance and output resistance. The M+1 by M input matrix **B** is

$$\mathbf{B} = \frac{V_{IN}}{N^2} \begin{bmatrix} \mathcal{R}_C + \mathcal{R}_L & \mathcal{R}_C & \cdots & \mathcal{R}_C \\ \mathcal{R}_C & \mathcal{R}_C + \mathcal{R}_L & \cdots & \mathcal{R}_C \\ \vdots & \vdots & \ddots & \vdots \\ \mathcal{R}_C & \mathcal{R}_C & \cdots & \mathcal{R}_C + \mathcal{R}_L \\ 0 & 0 & \cdots & 0 \end{bmatrix}, (12)$$

and the M+1 by M+1 output matrix **E** is

$$\mathbf{E} = \begin{bmatrix} 1 & 0 & \cdots & 0 & 0 \\ 0 & 1 & \cdots & 0 & 0 \\ \vdots & \vdots & \ddots & \vdots & \vdots \\ 0 & 0 & \cdots & 1 & 0 \\ R_c || R_o & R_c || R_o & \cdots & R_c || R_o & \frac{R_o}{R_o + R_c} \end{bmatrix} .$$
 (13)

We write the state matrix A in terms of constants for compactness and to highlight the symmetric upper-left submatrix and the identical elements in the other blocks. These properties of the symmetric converter will allow us to simplify the full state-space model in the proceeding subsections. A is time invariant and no state-space averaging is needed. Since the phases connected to V_{IN} change over time, the state-space averaging method [46] is used to find the input matrix B. The frequency range of the dynamic model is thus constrained to be much lower than the switching frequency. The bottom row of the output matrix E relates the output voltage to the capacitor voltage and phase currents.

B. Common-Mode Duty Cycle to Output Voltage Dynamics

We derive the transfer function from a common-mode duty cycle perturbation to the output voltage by taking a common-mode duty cycle input $d=d_1=d_2=\cdots=d_M$, and noting that the state-space average of all phase currents are equal in this case:

$$i_1 = i_2 = \dots = i_M, \tag{14}$$

$$i_T = \sum_{j=1}^{j=M} i_j = Mi_1.$$
 (15)

There are now only two independent state variables which we select as the capacitor output voltage v_c and the total current i_T . Equations (57) and (58) in Appendix II can be re-written in terms of the total output current i_T and the common-mode duty cycle input d as

$$\frac{di_T}{dt}\bigg|_{\text{average}} = v_c M \gamma + i_T (\alpha + (M-1)\beta) + \frac{V_{IN} M (M \mathcal{R}_C + \mathcal{R}_L)}{N^2} d,$$
(16)

$$\frac{dv_c}{dt} = v_c \rho + i_T \delta,\tag{17}$$

leading to a reduced order two-state state-space model:

$$\begin{bmatrix} \dot{i}_{T} \\ \dot{v}_{c} \end{bmatrix} = \underbrace{\begin{bmatrix} \alpha + (M-1)\beta & M\gamma \\ \delta & \rho \end{bmatrix}}_{\mathbf{A'}} \begin{bmatrix} i_{T} \\ v_{c} \end{bmatrix} + \underbrace{\frac{V_{IN}}{N^{2}}}_{\mathbf{M'}} \begin{bmatrix} M(M\mathcal{R}_{C} + \mathcal{R}_{L}) \\ 0 \end{bmatrix} d, \tag{18}$$

$$\begin{bmatrix} i_T \\ v_o \end{bmatrix} = \underbrace{\begin{bmatrix} 1 & 0 \\ R_c || R_o & \frac{R_o}{R_o + R_c} \end{bmatrix}}_{\mathbf{E}'} \begin{bmatrix} i_T \\ v_c \end{bmatrix}. \tag{19}$$

The state matrix \mathbf{A}' , input matrix \mathbf{B}' , and output matrix \mathbf{E}' have been modified to reflect the reduction of system order and single common-mode duty cycle input. We obtain the transfer function from a small-signal perturbation of the common-mode duty cycle \tilde{d} to the output voltage $\tilde{v_o}$ by converting the reduced order state-space model:

$$G_{\tilde{d} \to \tilde{v_o}}(s) = \frac{\tilde{v_o}}{\tilde{d}}(s) = (\mathbf{E}')_{\text{row } 2}(s\mathbf{I} - \mathbf{A}')^{-1}\mathbf{B}'$$
$$= \frac{MV_{IN}R_o(CR_cs + 1)}{H(s)}, \tag{20}$$

where

$$H(s) = CL_{l}(R_{o} + R_{c})s^{2} + [L_{l} + C(R_{w}R_{o} + R_{c}(MR_{o} + R_{w}))]s + (MR_{o} + R_{w}).$$
(21)

In equations (20) and (21), the reluctances are substituted with the expression for leakage inductance (3). In designs where the capacitor series resistance is negligible, the transfer function from the common-mode duty cycle to the output voltage is

$$\frac{\tilde{v_o}}{\tilde{d}}(s)\bigg|_{R_c=0} = \frac{MV_{IN}R_o}{CL_lR_os^2 + (L_l + CR_wR_o)s + (MR_o + R_w)}.$$
(22)

To the authors' knowledge, this is the first time the duty cycle to output voltage transfer function of the multiphase coupled inductor buck converter has been explicitly presented with reluctances, emphasizing the impact of the leakage inductance L_l on the dynamic behavior. The common-mode duty cycle to output voltage transfer function is second-order, regardless of the number of phases M. This property arises from the equal phase currents and resulting system order reduction in a symmetric converter with common-mode duty cycle control. Moreover, the leakage inductance L_l is a key element in this transfer function and the magnetizing inductance L_{μ} has no impact. When the duty cycles of all phases are changed uniformly, flux must travel through the center leg as illustrated in Fig. 3b, that is, the leakage path. If this path is low inductance, the converter has a fast transient response. The transfer function is equivalent to the duty cycle to output voltage transfer function of a multiphase buck converter with uncoupled inductors and L_l as the discrete inductance of each phase. For non-negligible capacitor series resistance R_c , the transfer function has a zero at $\omega = \frac{1}{R_c C}$. This zero may occur in a frequency range of interest if the capacitance and/or the series resistance are large. For negligible capacitor series resistance, the bandwidth ω_0 of the second-order system is

$$\omega_o = \sqrt{\frac{MR_o + R_w}{L_l C R_o}},\tag{23}$$

which may be increased by increasing the number of phases or reducing the leakage inductance L_l . The leakage inductance, expressed in equation (3), may be reduced by increasing the center leg reluctance \mathcal{R}_C . The bandwidth for converters with small winding resistance, $MR_o \gg R_w$, and high coupling coefficient, $M\mathcal{R}_C \gg \mathcal{R}_L$, may be approximated as

$$\omega_o \approx \frac{M}{N} \sqrt{\frac{\Re_C}{C}}.$$
 (24)

This indicates a linear dependence on the number of phases M and a square root dependence on leakage reluctance \mathcal{R}_C . Using many phases and a large reluctance \mathcal{R}_C , or even removing the center leg entirely, will increase system bandwidth.

C. Common-Mode Duty Cycle to Output Current Dynamics

The common-mode duty cycle to output current transfer function is useful for regulating the total converter current, such as when using inner loop current control. The winding current must also be regulated to avoid core saturation. We obtain the transfer function from a small-signal perturbation of the common-mode duty cycle \tilde{d} to the output current $\tilde{i_T}$ by converting the reduced order state-space model:

$$G_{\tilde{d} \to \tilde{i_T}} = \frac{\tilde{i_T}}{\tilde{d}}(s) = \begin{bmatrix} 1 & 0 \end{bmatrix} (s\mathbf{I} - \mathbf{A}')^{-1}\mathbf{B}'$$
$$= \frac{MV_{IN}(C(R_o + R_c)s + 1)}{H(s)}, \tag{25}$$

where H(s) is the same denominator defined in (21). This transfer function has the same two poles as the output voltage transfer function, having resulted from the same state-space model. As expected, it is equivalent to the duty cycle to output current transfer function of a multiphase buck converter with L_l as the discrete inductance of each phase. Similar to the output voltage dynamics, the leakage inductance L_l is a key element in this transfer function and the magnetizing inductance L_μ has no impact.

D. Differential Duty Cycle to Differential Current Dynamics

Individually controlling phase currents is challenging in coupled inductor circuits since changing the current of one phase will also affect the others. Individual control of phase currents can be intentional, such as in active current balancing, or unintentional, such as imbalances introduced by duty cycle offsets or input voltage variations in the middle of a switching period. One way to analyze the dynamics of phase current control is to divide the duty cycle control actions into common-mode and differential control of phase currents. Common-mode control refers to changing the total current by changing all duty cycles equally as covered in section III-C; differential control refers to controlling the difference between two phase currents by changing the difference between their duty cycles. Since the duty cycles of all phases are no longer identical, we consider the full state-space model. The upper left M by M submatrix of the state matrix \mathbf{A} in equation (6), denoted here as P, is

$$\mathbf{P} \coloneqq \begin{bmatrix} \alpha & \beta & \beta & \cdots & \beta \\ \beta & \alpha & \beta & \cdots & \beta \\ \beta & \beta & \alpha & \cdots & \beta \\ \vdots & \vdots & \vdots & \ddots & \vdots \\ \beta & \beta & \beta & \cdots & \alpha \end{bmatrix}. \tag{26}$$

The submatrix \mathbf{P} represents the phase current subspace, that is, it describes the evolution of phase currents with respect to each other with the output voltage held constant. As proven in [33], the output voltage remains constant when balancing the phase currents to an average. Therefore, we study the eigenstructure of \mathbf{P} to find a natural basis for the phase currents states that will simplify the dynamic equations of current balancing.

As shown in Appendix III, one set of eigenvectors of \mathbf{P} is $\mathbf{p_1} = \begin{bmatrix} 1,1,1,\ldots,1 \end{bmatrix}^T$ and $\mathbf{p_j} = \begin{bmatrix} 1,0,\ldots,0,-1,0,\ldots,0 \end{bmatrix}^T$ for $j=2\ldots M$, where element j of $\mathbf{p_j}$ is -1. The $\mathbf{p_1}$ eigenvector represents the total current, $i_1+i_2+\cdots+i_M$, and has associated eigenvalue $\lambda_1=\alpha+(M-1)\beta$. Each of the $\mathbf{p_j}$ eigenvectors represents the difference between phase current i_1 and phase current i_j , i_1-i_j , with repeated eigenvalues

 $\lambda_j = \alpha - \beta$. If we write a matrix **V** with the eigenvectors as the columns,

$$\mathbf{V} := \begin{bmatrix} 1 & 1 & 1 & \cdots & 1 \\ 1 & -1 & 0 & \cdots & 0 \\ 1 & 0 & -1 & \cdots & 0 \\ \vdots & \vdots & \vdots & \ddots & \vdots \\ 1 & 0 & 0 & \cdots & -1 \end{bmatrix}, \tag{27}$$

we can use V to diagonalize P and and transform the phase current states to total current and differential current components. To transform the full state-space model that includes the capacitor voltage state, we define a transform matrix

$$\mathbf{T} = \begin{bmatrix} \mathbf{V} & \mathbf{0}_{1 \times M} & \mathbf{0}_{M \times 1} \\ \mathbf{0}_{1 \times M} & \mathbf{1} & \mathbf{1} \end{bmatrix}, \tag{28}$$

and a transformed vector of states $\boldsymbol{\xi}$:

$$\boldsymbol{\xi} = \mathbf{T}\mathbf{x} = \begin{bmatrix} \mathbf{V} & \mathbf{0}_{1 \times M} & \mathbf{0}_{M \times 1} \\ \mathbf{0}_{1 \times M} & \mathbf{1} \end{bmatrix} \begin{bmatrix} i_1 \\ i_2 \\ \vdots \\ i_M \\ v_c \end{bmatrix} = \begin{bmatrix} i_T \\ i_1 - i_2 \\ \vdots \\ i_1 - i_M \\ v_c \end{bmatrix}. \quad (29)$$

The ${\bf T}$ matrix transforms the original capacitor voltage and M phase current states to a new set of states consisting of the capacitor voltage, total current, and M-1 current differences. To apply a similar transformation to the input matrix ${\bf B}$, we consider the upper M by M submatrix of ${\bf B}$, denoted as ${\bf R}$:

$$\mathbf{R} := \frac{V_{IN}}{N^2} \begin{bmatrix} \mathcal{R}_C + \mathcal{R}_L & \mathcal{R}_C & \cdots & \mathcal{R}_C \\ \mathcal{R}_C & \mathcal{R}_C + \mathcal{R}_L & \cdots & \mathcal{R}_C \\ \vdots & \vdots & \ddots & \vdots \\ \mathcal{R}_C & \mathcal{R}_C & \cdots & \mathcal{R}_C + \mathcal{R}_L \end{bmatrix} . (30)$$

 ${f R}$ represents the effect of the input duty cycles on the phase current states and has the same structure as ${f P}$ in equation (26), so it can be diagonalized with the same matrix of eigenvectors ${f V}$. The duty cycle input vector is transformed into a new input vector ${f q}$ which consists of the sum of all duty cycles and the duty cycle differences:

$$\mathbf{q} = \mathbf{V}\mathbf{u} = \mathbf{V} \begin{bmatrix} d_1 \\ d_2 \\ \vdots \\ d_M \end{bmatrix} = \begin{bmatrix} d_1 + d_2 + \dots + d_M \\ d_1 - d_2 \\ \vdots \\ d_1 - d_M \end{bmatrix}. \tag{31}$$

Substituting the new state and input vectors $\mathbf{x} = \mathbf{T}^{-1}\boldsymbol{\xi}$ and $\mathbf{u} = \mathbf{V}^{-1}\mathbf{q}$ in the original state equation (4), we obtain a transformed state-space model with equations in terms of the differential currents and differential duty cycles

$$\dot{\boldsymbol{\xi}} = \mathbf{T}\mathbf{A}\mathbf{T}^{-1}\boldsymbol{\xi} + \mathbf{T}\mathbf{B}\mathbf{V}^{-1}\mathbf{q},\tag{32}$$

where

$$\mathbf{TAT^{-1}} = \begin{bmatrix} \lambda_{1} & 0 & \cdots & 0 & M\gamma \\ -0 & \lambda_{2} & \cdots & 0 & 0 & 0 \\ \vdots & \vdots & \vdots & \vdots & \vdots & \vdots \\ 0 & 0 & \cdots & \lambda_{M-1} & 0 & 0 \\ 0 & 0 & \cdots & 0 & \lambda_{M} & 0 \\ -\delta & 0 & \cdots & 0 & \lambda_{M} & 0 \\ -\delta & 0 & \cdots & 0 & 0 & \rho \end{bmatrix}$$
(33)

TABLE IV
RELUCTANCE-BASED TRANSFER FUNCTIONS OF THE MULTIPHASE
COUPLED INDUCTOR BUCK CONVERTER

	Common-Mode Transfer Function			
$\frac{\tilde{v_o}}{\tilde{d}}$	$\frac{MV_{IN}R_{o}(CR_{c}s+1)}{CL_{l}(R_{o}+R_{c})s^{2}+[L_{l}+C(R_{w}R_{o}+R_{c}(MR_{o}+R_{w}))]s+(MR_{o}+R_{w})}$			
$\frac{\tilde{i_T}}{\tilde{d}}$	$\frac{MV_{IN}(C(R_o + R_c)s + 1)}{CL_l(R_o + R_c)s^2 + [L_l + C(R_w R_o + R_c(MR_o + R_w))]s + (MR_o + R_w)}$			
	Differential-Mode Transfer Function			
$\frac{\Delta \tilde{i}}{\Delta \tilde{d}}$	$rac{V_{IN} \mathcal{R}_L}{sN^2 + R_w \mathcal{R}_L}$			

TABLE V

SIMPLIFIED TRANSFER FUNCTIONS OF THE MULTIPHASE COUPLED INDUCTOR BUCK CONVERTER ASSUMING $R_c=0$ and $R_w=0$

	Simplified Common-Mode Transfer Function	
$\frac{\tilde{v_o}}{\tilde{d}}$	$\frac{MV_{IN}R_o}{CL_lR_os^2 + L_ls + MR_o}$	
$rac{i_T^{ ilde{}}}{ ilde{d}}$	$\frac{MV_{IN}(CR_os+1)}{CL_lR_os^2+L_ls+MR_o}$	
	Simplified Differential-Mode Transfer Function	
$\frac{\Delta \tilde{i}}{\Delta \tilde{d}}$	$rac{V_{IN}\mathcal{R}_L}{sN^2}$	

and

$$\mathbf{TBV^{-1}} = \frac{V_{IN}}{N^2} \begin{bmatrix} -\frac{M\mathcal{R}_C + \mathcal{R}_L}{0} & \frac{0}{\mathcal{R}_L} & \cdots & \frac{0}{0} & \frac{0}{0} \\ \vdots & \vdots & \ddots & \vdots & \vdots \\ 0 & \vdots & 0 & \cdots & \mathcal{R}_L & 0 \\ -\frac{0}{0} & -\frac{1}{0} & \frac{0}{0} & \cdots & \frac{0}{0} & \frac{\mathcal{R}_L}{0} \end{bmatrix}.$$
(34)

Extended derivations for (33) and (34) are provided in Appendix III.

Inspecting the rows and columns of (33) and (34) relating to the differential current states ξ_2,\ldots,ξ_M , we can see that the dynamic equations of each of the differential currents are independent from the equations of the total current ξ_1 and capacitor voltage ξ_{M+1} . Moreover, the differential current equations are decoupled from each other. For example, if the differential duty cycle $q_2=d_1-d_2$ is changed, the differential current $\xi_2=i_1-i_2$ will be affected independent of all other states. One can control the differential current states ξ_2,\ldots,ξ_M to zero to balance the phase currents.

All the eigenvalues associated with the differential currents are equal to $\lambda_j = \alpha - \beta = -\frac{\Re_L R_w}{N^2}$. As a result, all the differential currents can be described by the same differential equation

$$\dot{\xi}_{j} = \frac{d(i_{1} - i_{j})}{dt} = -\frac{\mathcal{R}_{L}R_{w}}{N^{2}}(i_{1} - i_{j}) + \frac{V_{IN}\mathcal{R}_{L}}{N^{2}}(d_{1} - d_{j}),$$
(35)

for any $j=2,\ldots,M$. This is a first-order equation and the transfer function is

$$\frac{\tilde{\xi}_j}{\tilde{q}_j}(s) = \frac{\tilde{i}_1 - \tilde{i}_j}{\tilde{d}_1 - \tilde{d}_j}(s) = \frac{\frac{V_{IN}\mathcal{R}_L}{N^2}}{s + \frac{R_w\mathcal{R}_L}{N^2}} = \frac{V_{IN}\mathcal{R}_L}{sN^2 + R_w\mathcal{R}_L}, \quad (36)$$

which depends only on the winding resistance R_w , side leg reluctance \mathcal{R}_L (magnetizing flux path), input voltage V_{IN} , and

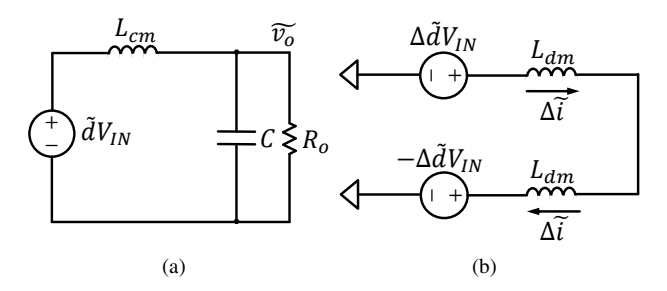


Fig. 5. Equivalent (a) common-mode dynamic model and (b) differential mode dynamic model for the multiphase coupled inductor buck converter. Circuit averaging is used to simplify the dynamic models [46].

number of turns N. It is independent of center leg reluctance (leakage flux path), capacitance, capacitor series resistance, and load resistance. Any purely differential current generates equal and opposite flux in two legs that does not flow through the leakage path and is not affected by the leakage inductance or center leg reluctance. There is a pole at $\omega = -\frac{R_w \mathcal{R}_L}{N^2}$, so differential currents decay faster for higher winding resistance R_w or side leg reluctance \mathcal{R}_L , analogous to a first-order system. For tightly coupled inductors $(M\mathcal{R}_C\gg\mathcal{R}_L)$ with a high number of phases M, the magnetizing inductance L_μ is approximately $\frac{N^2}{\mathcal{R}_L}$. The magnetizing inductance determines the differential current dynamics.

Equation (36) reveals a design tradeoff between the amplitude and settling time of differential currents in response to a disturbance. If \mathcal{R}_L is increased, current imbalances will settle faster, but they will be of greater initial amplitude. For example, if the duty cycles are constant but the input voltage amplitude is perturbed, one phase may be driven with a higher average voltage than the other and cause a current imbalance, as shown in [34]. This is an important design consideration to avoid core saturation during transient events. The reluctance-based transfer functions for all common-mode and differential-mode control cases are summarized in Table IV, with simplified versions assuming $R_c = R_w = 0$ listed in Table V.

E. Equivalent Models with Discrete Inductors

The common-mode dynamic model of a multiphase coupled inductor buck converter as shown in Fig. 5a can be interpreted as a single-phase buck converter with a discrete equivalent inductance

$$L_{cm} = \frac{L_l}{M} = \frac{N^2}{M(M\mathcal{R}_C + \mathcal{R}_L)},\tag{37}$$

assuming $R_w=R_c=0$. The transfer function is similar to that of a single-phase buck converter [47]:

$$\frac{\tilde{v_o}}{\tilde{d}} = \frac{V_{IN}R_o}{CL_{cm}R_os^2 + L_{cm}s + R_o}$$
(38)

Therefore, the common-mode dynamics of the multiphase coupled inductor buck converter may be designed the same way as a single-phase buck with equivalent inductance L_{cm} . The differential-mode dynamic model of the multiphase coupled inductor buck converter as shown in Fig. 5b can be interpreted as multiphase uncoupled buck converter with a discrete equivalent inductance

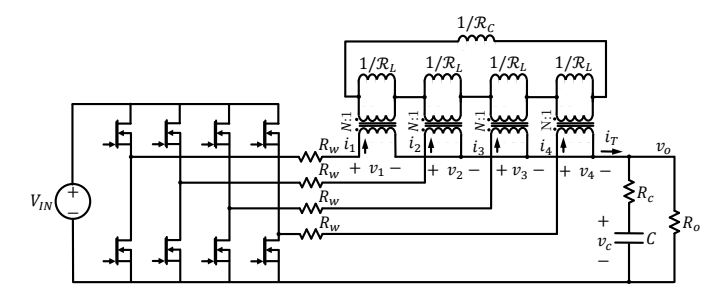


Fig. 6. Schematic of a four-phase coupled inductor buck converter used to verify the predicted common-mode and differential-mode dynamics. The coupled inductor is represented with the inductance dual model. The component values of this design are listed in Table VI.

$$L_{dm} = \frac{N^2}{\Re_L} \approx L_{\mu} \tag{39}$$

for each phase, assuming tight coupling and a high number of phases. The transfer function is similar to that of a multiphase uncoupled buck converter:

$$\frac{\Delta \tilde{i}}{\Delta \tilde{d}} = \frac{V_{IN}}{sL_{dm}}.$$
(40)

Therefore, the differential-mode dynamics of the multiphase coupled inductor buck converter may be designed the same way as a multiphase uncoupled inductor buck converter with equivalent inductance L_{dm} .

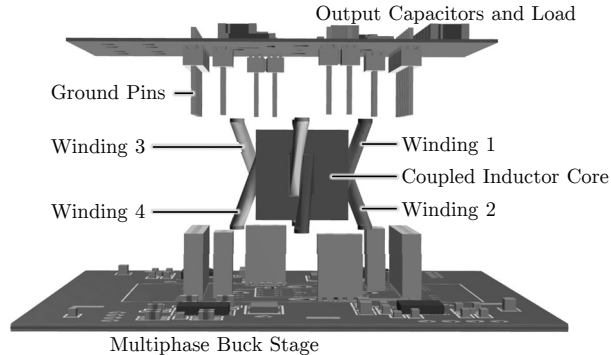
We apply the inductance dual model to reveal the dynamic behavior of the multiphase coupled inductor buck converter, but the same approach is also applicable to other basic circuits such as boost or buck-boost converters. The dynamic equations still originate from the inductance dual model in equation (1), though a new state-space model must be derived for other converters; for example, a boost converter has a different state matrix A that is time varying, unlike the buck converter. Assuming the converter is also symmetric, the new state-space model can be similarly simplified to find the transfer functions.

IV. TEST PLATFORM FOR THE RELUCTANCE-BASED DYNAMIC MODELS

A four-phase buck converter with the schematic shown in Fig. 6 is used to verify the theoretical results. 3D renders and images of the converter assembly implementing a vertical coupled inductor structure are shown in Fig. 7. The vertical structure is especially suitable for vertical power delivery in point-of-load converters [5], [14], [48], [49] where the load is on a board above the switching stage. The coupled inductor with four windings wrapped around the side legs is interposed between two boards and the windings are soldered to both boards. Four Infineon TDA Series DrMOS are used for the switching stage on the bottom board. The output capacitors and load resistors are placed on the top board.

A custom four-phase core is fabricated with Ferroxcube 3F4 material [50], which has a saturation flux density of 410 mT at 25 °C and a relative permeability of approximately 900. One turn (N = 1) is used for every phase. The custom-made symmetric core is pictured and dimensioned in Fig. 8.

Figure 9 shows the ripple current of each phase with the circuit operating at a 1 MHz switching frequency, 12 V input



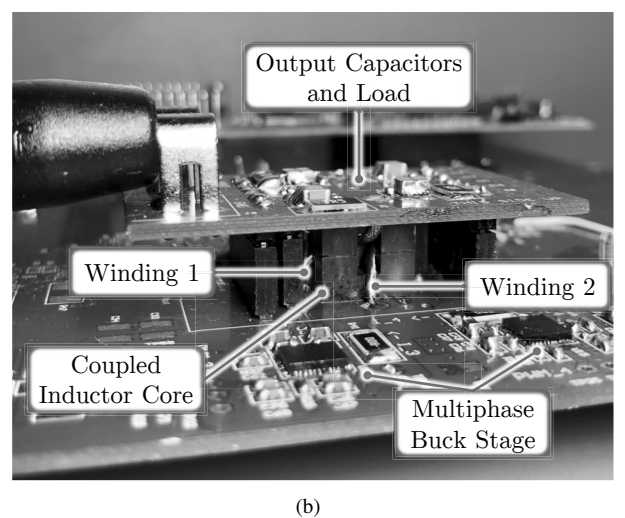


Fig. 7. (a) Exploded view and (b) image of the four-phase coupled inductor buck converter. The core is interposed between the two boards with a 20 AWG winding wrapped around each of the side legs.

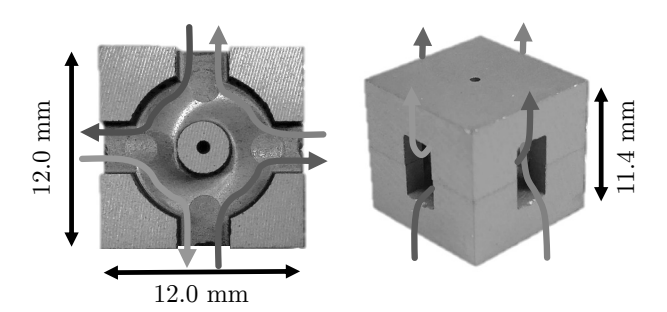


Fig. 8. Top and isometric view of the core illustrating four winding paths with one turn each. Two identical halves are put together to form the core. The side legs have an area of 14.9 mm² and the center leg has an area of 6.61 mm². Based on the measured reluctances, the effective path lengths of the side and center legs are 9.54 mm and 6.09 mm respectively.

voltage, and 1.5 V output voltage. The ripple frequency is multiplied to 4 MHz due to the coupling between phases. The center leg reluctance, side leg reluctance, and leakage inductance are determined from the slope of the current ripple. From equation (1), it may be shown that when phase k is connected to V_{IN} while the others are off, its current ramps up with slope

$$\frac{di_k}{dt}\Big|_{up} = (\mathcal{R}_C + \mathcal{R}_L)V_{IN} - (M\mathcal{R}_C + \mathcal{R}_L)v_o, \tag{41}$$

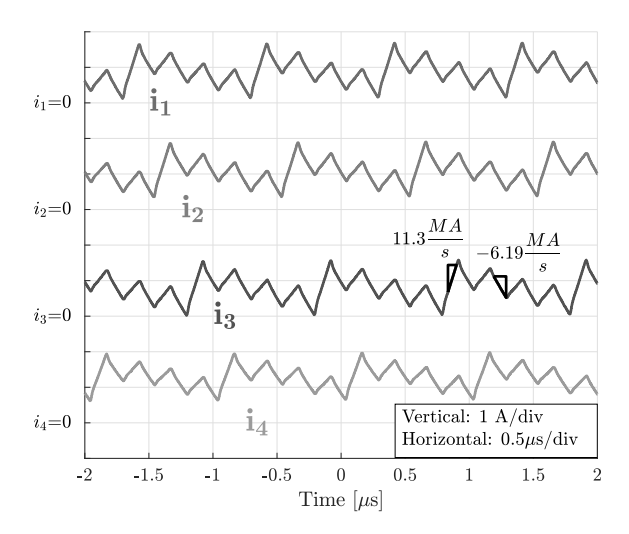


Fig. 9. Phase current ripple measured by a current probe with input voltage $V_{IN}=12$ V, output voltage $v_o=1.5$ V, and switching frequency $f_{sw}=1$ MHz. The coupling effect multiplies the phase current ripple frequency to 4 MHz. The measured phase current slopes are used to experimentally determine the core reluctances.

and when all phases are off, its current ramps down with slope

$$\frac{di_k}{dt}\bigg|_{\text{down}} = -(M\mathcal{R}_C + \mathcal{R}_L)v_o,\tag{42}$$

for $k = 1 \dots M$. The phase current slopes of all four phases are recorded as illustrated in Fig. 9 and the reluctances \mathcal{R}_C , \mathcal{R}_L are determined with (41) and (42). The average \mathcal{R}_C and \mathcal{R}_L are computed and the leakage inductance is found using equation (3). Table VI lists the measured center leg reluctance \mathcal{R}_C , side leg reluctance \mathcal{R}_L , capacitance C, capacitor series resistance R_c , winding resistance R_w , and other circuit parameters. 4, 8, or 16 Murata 220 µF X5R ceramic capacitors are put in parallel for the output capacitance. The capacitance and series resistance are measured using an HP 4192A impedance analyzer with the capacitors soldered incircuit under a 1.5 V dc bias. The capacitor series resistance R_c varies significantly with frequency. Therefore, we measure R_c across the frequency sweep range, as shown in Fig. 10, and change the values in the computation of theoretical curves as the frequency changes. The series resistance values recorded in Table VI are the minimum values in the frequency range. The measurement includes PCB trace resistance, which is highest when 16 capacitors are connected. While this higher resistance will impact converter performance, it serves as a useful example for model verification. The winding resistance R_w is similarly measured in-circuit and includes all trace resistance and wire resistance between the switch node and output capacitors. The efficiency is recorded for various operating conditions in Fig. 11.

V. SIMULATIONS AND EXPERIMENTAL VERIFICATIONS

To verify the theoretical transfer functions, we compare them to simulated results from PSIM and experimental results. The frequency response is experimentally measured using the setup illustrated in Fig. 12. An oscilloscope (Tektronix

TABLE VI CIRCUIT PARAMETERS OF THE TEST PLATFORM

Parameter	Value
Input Voltage V_{IN}	12 V
Output Voltage v_o	1.5 V
Switching Frequency f_{sw}	1 MHz
Output Load Resistance R_o	0.375Ω
Center Leg Reluctance \Re_C	$814 \times 10^3 \text{ H}^{-1}$
Side Leg Reluctance \mathcal{R}_L	$566 \times 10^3 \text{ H}^{-1}$
Leakage Inductance L_l	262 nH
4 Parallel C_{out} Capacitance C	491 μF
8 Parallel C_{out} Capacitance C	$976~\mu F$
16 Parallel C_{out} Capacitance C	$2020~\mu F$
4 Parallel C_{out} Series Resistance R_c	0.9 mΩ
8 Parallel C_{out} Series Resistance R_c	$0.9~\mathrm{m}\Omega$
16 Parallel C_{out} Series Resistance R_c	$2.3~\text{m}\Omega$
Winding Resistance R_w	8.9 mΩ

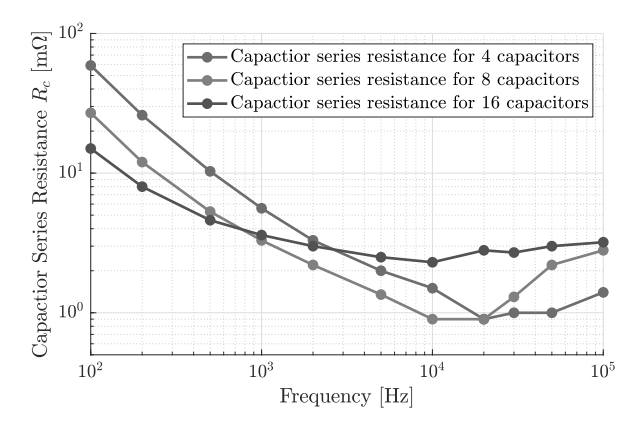


Fig. 10. Measured capacitor series resistance R_c for 4, 8, and 16 parallel output capacitors intended for model verification. The capacitors are soldered in circuit and a 1.5 V dc bias is applied when the series resistance is measured. PCB trace resistances are included in these measurements.

MSO58) generates a sinusoidal perturbation which is measured by the microcontroller (TI TMS320F28069M). The duty cycles of the 1 MHz PWM signals are perturbed $\pm 1\%$ at this frequency. The switch node of phase 1, which has a 1 MHz PWM component and a small signal duty cycle perturbation, is put through an analog band-pass filter. This removes the high frequency PWM component and the dc component, isolating the duty cycle perturbation to be measured by channel 1 of the oscilloscope. Depending on which transfer function is being verified, the output voltage v_o , total current i_T , or differential current i_1-i_3 is measured by channel 2 of the oscilloscope. The gain and phase between channels 1 and 2 are computed for perturbation frequencies from 10 Hz to 100 kHz to generate a bode plot of the chosen transfer function.

The switches are operated at 1 MHz and the duty cycle refresh rate is about 450 kHz. The duty cycle update of each phase occupies the bulk of the control loop time in the microcontroller. Since we measure only switch node 1 and phase 1 is updated before the other three, an effective time delay is introduced to the phase measurements. To capture this delay, an exponential time delay term of 1.7 μ s (the duration of the duty cycle update) is added to the theoretical

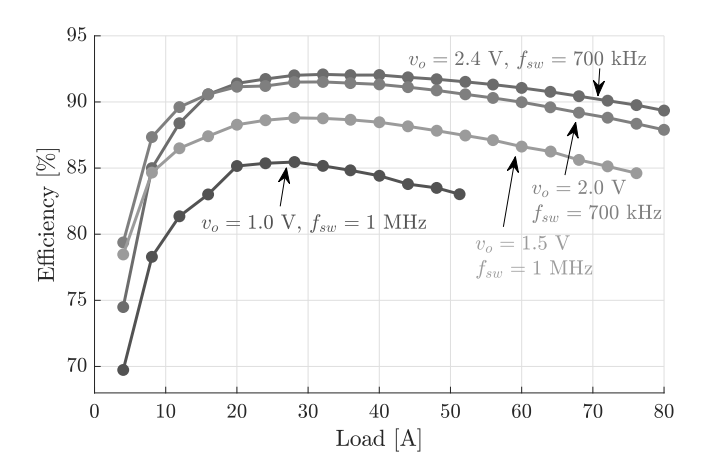


Fig. 11. Measured efficiency of the experimental setup with $V_{IN}=12~{\rm V}.$ Better efficiency is achieved for lower step-down ratios and lower switching frequencies.

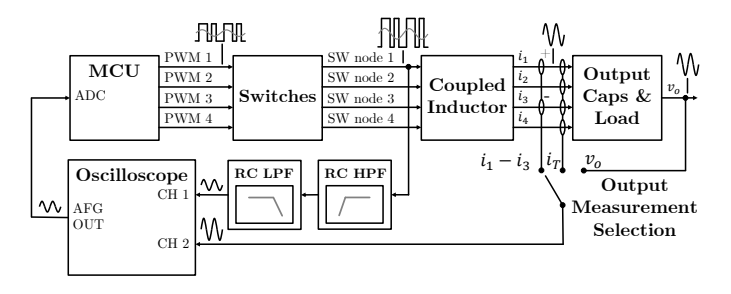


Fig. 12. Block diagram illustrating the frequency response measurement technique. After analog filtering, the switch node of phase 1 is measured as the small signal duty cycle perturbation. The differential current i_1-i_3 , total current i_T , or output voltage v_o is measured depending on the transfer function being verified.

transfer functions when a common-mode duty cycle input is used. When the duty cycles of phase 1 and 3 are perturbed deferentially and switch node 1 is measured as the input, the gain is corrected with a factor of 2 because only half of the total perturbation is measured.

A. Common-Mode Duty Cycle to Output Voltage Dynamics

Figure 13 shows the measured, simulated, and theoretical frequency response from a common-mode duty cycle perturbation to the output voltage with 4, 8, and 16 parallel output capacitors. All four duty cycles are perturbed identically and synchronously to verify the dynamic response predicted in equation (20). Figure 14 shows the measured output voltage response to a step change in the duty cycle with 8 parallel output capacitors. The zoomed-in figure shows the output voltage ripple.

B. Common-Mode Duty Cycle to Output Current Dynamics

Figure 15 compares the measured, simulated, and theoretical frequency response from a common-mode duty cycle to the total output current transfer function with 4, 8, and 16 parallel output capacitors. Figure 16 shows the output current response to a step change in the duty cycle with 8 parallel output capacitors. The high gain for rapid changes in the duty cycle

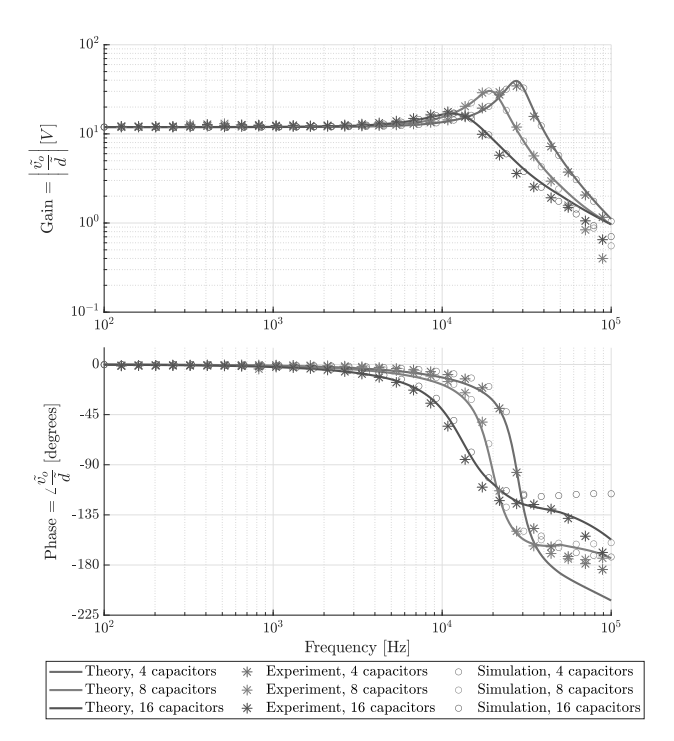


Fig. 13. Comparison of measured, simulated, and theoretical transfer functions from a common-mode duty cycle perturbation to the output voltage with 4, 8, and 16 parallel output capacitors.

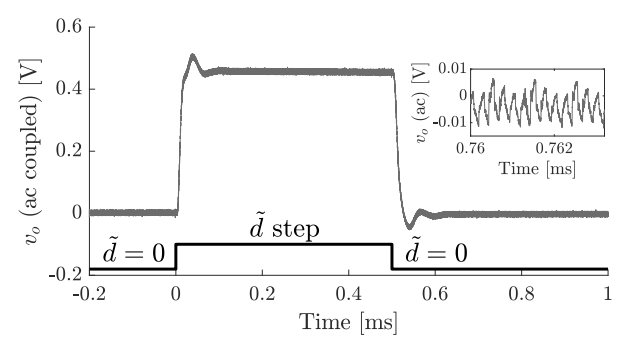


Fig. 14. Measured output voltage response to a step change of the duty cycle lasting for 0.5 ms with 8 parallel output capacitors.

(high frequencies) and low dc gain are reflected in the transient response. The zoomed-in figure shows the total current ripple.

C. Differential Duty Cycle to Differential Current Dynamics

Figure 17 compares the measured, simulated, and theoretical frequency response from a differential duty cycle input to the differential current. The experiments are performed with the winding resistance recorded in Table VI and with a 50 m Ω or $100~\text{m}\Omega$ resistor added in series with every winding.

Figure 18 shows the measured phase current responses to a differential step change in the duty cycles of phases 1 and 3 while the duty cycles of phases 2 and 4 are held constant. Phase currents 2 and 4 do not change while phase currents 1 and 3 exhibit an exponential response in equal and opposite directions, which is characteristic of a first-order system. The zoomed-in figure shows the phase 1 current ripple.

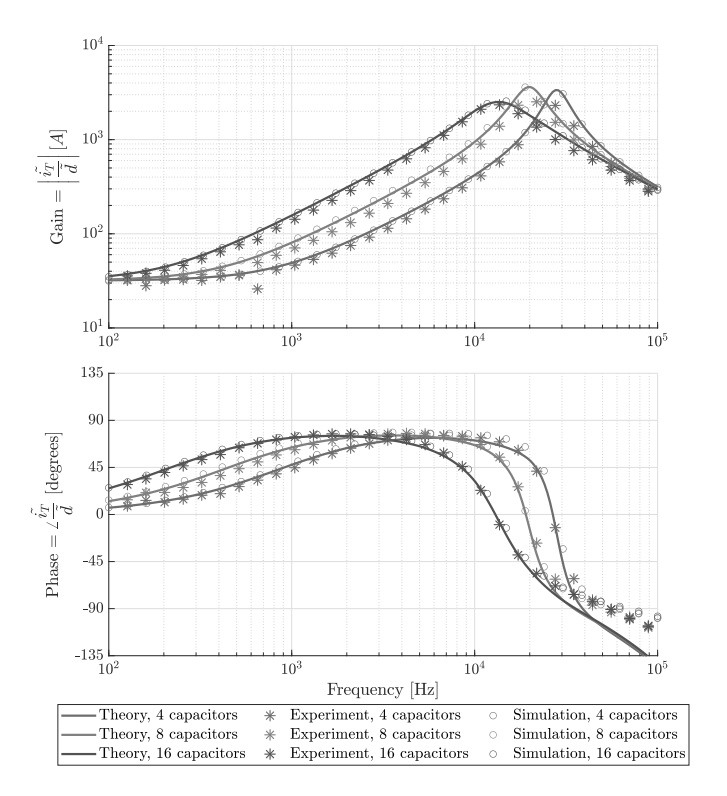


Fig. 15. Comparison of measured, simulated, and theoretical transfer functions from a common-mode duty cycle perturbation to the total output current with 4, 8, and 16 parallel output capacitors.

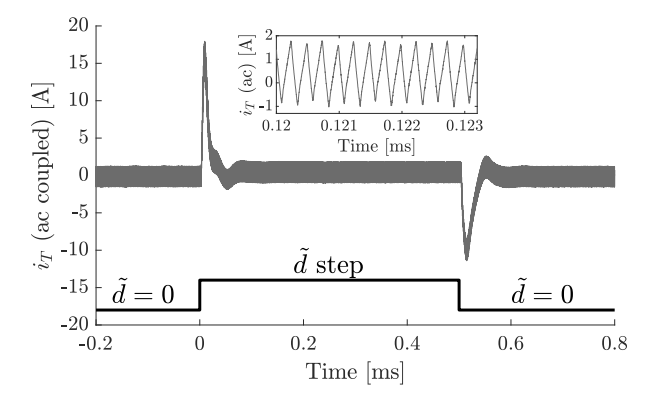


Fig. 16. Measured output current response to a step change of the duty cycle lasting for 0.5 ms with 8 parallel output capacitors.

D. Differential Current Imbalance after an Input Voltage Step

To illustrate the tradeoff between current imbalance amplitude and settling time, we consider a transient phase current imbalance caused by a change in the input voltage. Assuming the input voltage changes during time $t \in [dT, \frac{T}{M}]$ for $d < \frac{1}{M}$, phase 1 is driven with the old voltage, $V_{IN,OLD}$, and phase 2 is driven with the new voltage, $V_{IN,NEW}$. For an M phase design, a current imbalance of initial amplitude

$$\Delta(i_1 - i_2) = \frac{dT \mathcal{R}_L(M - 1)}{M} (V_{IN,OLD} - V_{IN,NEW})$$
 (43)

will be generated, as derived in Appendix IV. The amplitude scales linearly with \mathcal{R}_L and the settling time is inversely related to \mathcal{R}_L , illustrating the trade-off between imbalance

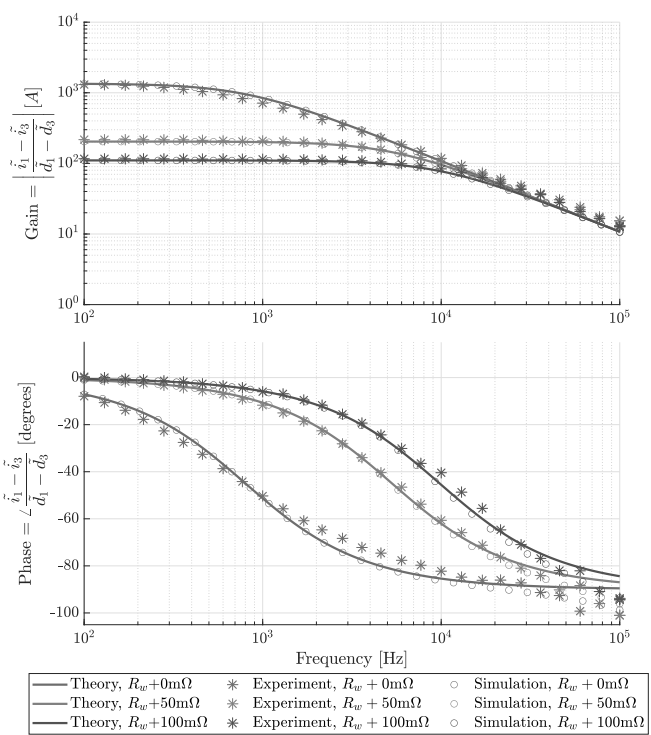


Fig. 17. Comparison of measured, simulated, and theoretical transfer functions from a differential duty cycle perturbation $\tilde{d_1} - \tilde{d_3}$ to the differential current $\tilde{i_1} - \tilde{i_3}$. The results agree when the base winding resistance R_w is used and when series resistors are added to the windings.

TABLE VII
CURRENT IMBALANCE AMPLITUDE AND DECAY TIME CONSTANT

Side Leg Reluctance \mathcal{R}_L	Imbalance Amplitude	Decay Time Constant
$283 \times 10^{3} \; \mathrm{H}^{-1}$	0.955 A	0.397 ms
$566 \times 10^{3} \; \mathrm{H}^{-1}$	1.91 A	0.199 ms
$1132 \times 10^3 \; \mathrm{H}^{-1}$	3.82 A	0.099 ms

amplitude and settling time. In Fig. 19, the differential current imbalance $\Delta(i_1-i_2)$ is plotted after an input voltage step from $V_{IN,OLD}=48~{\rm V}$ to $V_{IN,NEW}=12~{\rm V}$ in between phases 1 and 2 for a four-phase converter. For the side leg reluctances analyzed, the expected decay time constants and imbalance amplitudes are listed in Table VII, which have good agreement with the simulated results. Increasing \mathcal{R}_L decreases the magnetizing inductance L_μ , which increases ripple and the initial imbalance, but it also reduces the time taken for the imbalance to decay. If one needs to limit the amplitude of imbalance, for example, to avoid saturation of one phase, a smaller \mathcal{R}_L may be chosen. Or, if the imbalance must decay faster, a larger \mathcal{R}_L may be selected instead.

VI. APPLICABILITY AND LIMITATIONS

The dynamic models presented in this paper are derived by assuming the magnetic structure is symmetric such that all windings have uniform coupling relationships with other windings. Variations in the side and center leg reluctances may arise from manufacturing variations, magnetic material

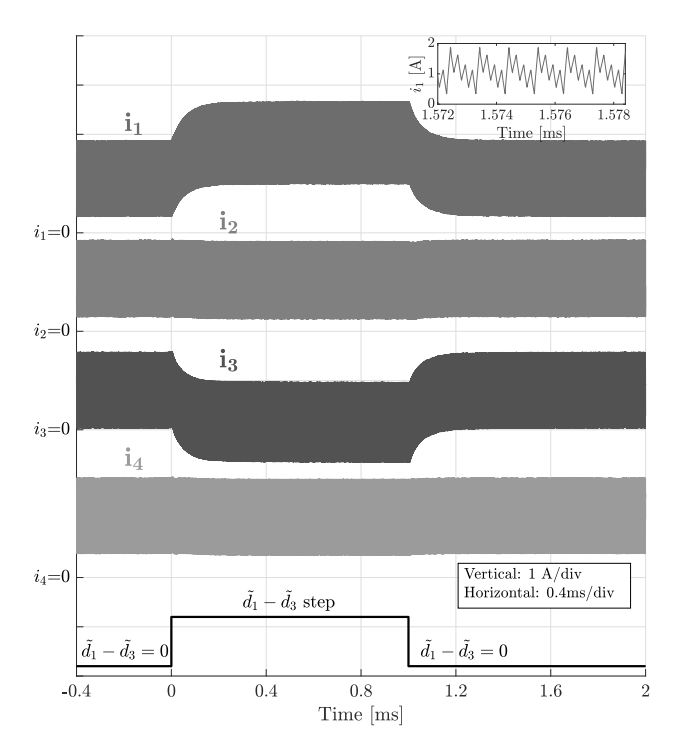


Fig. 18. Phase current response to a differential step in the duty cycles d_1 and d_3 . Phase currents i_1 and i_3 are perturbed in opposite directions and exhibit an exponential response. The duty cycles of phases 2 and 4 are held constant and their phase currents remain constant.

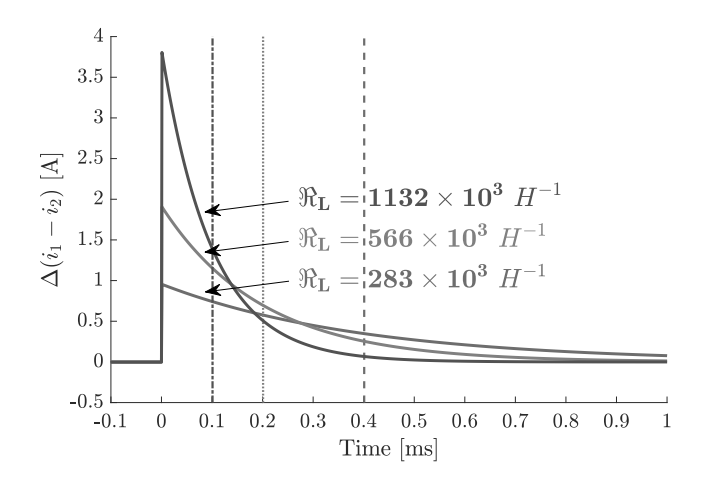


Fig. 19. Simulated settling of differential current imbalance generated by an input voltage step in between switching of the first and second phases of a four-phase converter. The differential current decays exponentially, with higher initial amplitude and faster settling for higher side leg reluctance \mathcal{R}_L . The time constants are denoted by dotted vertical lines.

variations, thermal expansion, or physical damage to the core. We discuss the applicability and limitations of the dynamic models by analyzing the sensitivity of the transfer functions to reluctance asymmetry.

Figures 20a and 20b plot the frequency response from a common-mode duty cycle input to the output voltage for variations in one of the four side leg reluctances \mathcal{R}_{L1} and variations in the center leg reluctance \mathcal{R}_{C} . All other reluctances are kept the same. The transfer function is not significantly affected by large variations in \mathcal{R}_{L1} , but it varies significantly with changes

in \mathcal{R}_C . A larger \mathcal{R}_C leads to higher system bandwidth. The differential-mode transfer function is independent of \mathcal{R}_C but varies significantly with \mathcal{R}_{L1} , as shown in Fig. 20c.

The common-mode dynamic models require a precise value of the center leg reluctance \mathcal{R}_C since the leakage flux path is primarily determined by \mathcal{R}_C , but these models are robust to asymmetries in side leg reluctances (magnetizing reluctance paths). The differential-mode dynamic model is independent of \mathcal{R}_C but is sensitive to variations in the side leg reluctances \mathcal{R}_L , which determine the magnetizing flux path.

In summary, asymmetries of the side leg reluctances (magnetizing path) have a negligible impact on the common-mode dynamics of a multiphase coupled inductor buck converter and have a major impact on the differential mode dynamics. Variations in the center leg reluctance (leakage path) significantly affect the common-mode dynamics and do not impact on the differential mode behavior of the multiphase coupled inductor buck converter. These results support the feasibility of scaling coupled inductor structures to a large number of phases and side legs with tolerance for asymmetry.

VII. CONCLUSION

This paper investigates dynamic models for multiphase coupled inductor buck converters based on magnetic reluctances and the inductance dual model. This approach connects the dynamic characteristics of a multiphase coupled inductor in the circuit domain and magnetic domain and offers key design insights for coupled inductor design. A complete state-space model and transfer functions are derived for the first time for an M-phase coupled inductor buck converter for commonmode and differential-mode transfer function analysis. For common-mode duty cycle control, it is shown that the control to output voltage and total current transfer functions are second-order, regardless of the number of phases, and that the transfer functions are determined by the leakage flux path and the leakage inductance L_l . We explore the dynamics of current balancing controlled by differential duty cycles, which simplifies the current balancing problem to a decoupled first-order system determined only by winding resistance and magnetizing flux path. The applicability and limitations of these dynamic models are discussed. The models are verified by SPICE simulations and experimental measurements.

APPENDIX I RELATION BETWEEN CORE RELUCTANCES AND MAGNETIZING AND LEAKAGE INDUCTANCES

The magnetizing inductance L_{μ} describes the flux generated in one leg that passes through the other side legs. The leakage inductance L_l describes the remaining flux that leaks through other reluctance paths. We consider the schematic in Fig. 21a, where all but one of the coils are open-circuited such that the currents are zero and the MMF sources are shorted. This may be reduced to Fig. 21b, where the magnetizing flux Φ_1 and

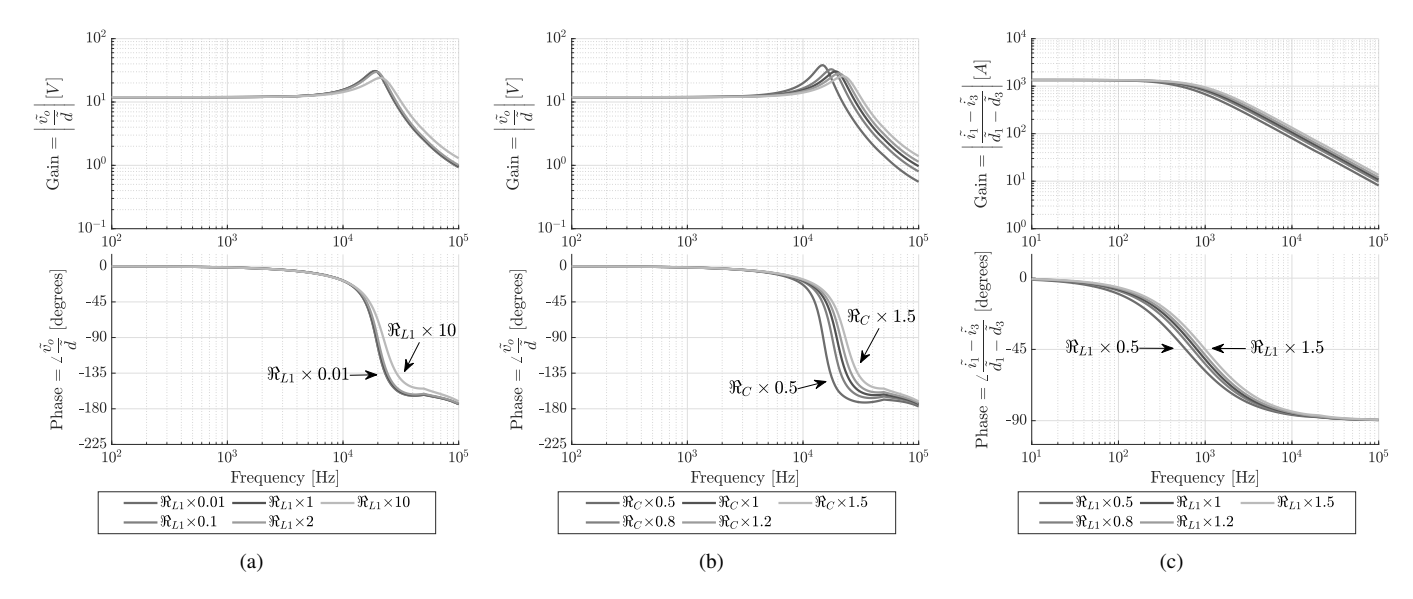


Fig. 20. Theoretical transfer function from (a) common-mode duty cycle to output voltage for varying values of one of the four side leg reluctances \mathcal{R}_{L1} , (b) common-mode duty cycle to output voltage for varying values of the center leg reluctance \mathcal{R}_C , and (c) differential-mode duty cycle to phase current difference for varying values of one of the four side leg reluctances \mathcal{R}_{L1} . In this experiment, $\mathcal{R}_L = 566 \times 10^3 \text{ H}^{-1}$ and $\mathcal{R}_C = 814 \times 10^3 \text{ H}^{-1}$.

leakage flux Φ_2 are denoted. The total flux induced by $\operatorname{coil}\ 1$ is

$$\Phi_1 + \Phi_2 = \frac{Ni_1}{\mathcal{R}_L + \mathcal{R}_C || \frac{\mathcal{R}_L}{M-1}}$$

$$= \frac{Ni_1(\mathcal{R}_L + (M-1)\mathcal{R}_C)}{\mathcal{R}_L(M\mathcal{R}_C + \mathcal{R}_L)}.$$
(44)

Applying the current divider rule, we find

$$\Phi_{1} = \frac{Ni_{1}(\mathcal{R}_{L} + (M-1)\mathcal{R}_{C})}{\mathcal{R}_{L}(M\mathcal{R}_{C} + \mathcal{R}_{L})} \times \frac{\mathcal{R}_{C}}{\mathcal{R}_{C} + \frac{\mathcal{R}_{L}}{M-1}}$$

$$= \frac{Ni_{1}(M-1)\mathcal{R}_{C}}{\mathcal{R}_{L}(M\mathcal{R}_{C} + \mathcal{R}_{L})},$$
(45)

and

$$\Phi_2 = \frac{Ni_1(\mathcal{R}_L + (M-1)\mathcal{R}_C)}{\mathcal{R}_L(M\mathcal{R}_C + \mathcal{R}_L)} \times \frac{\frac{\mathcal{R}_L}{M-1}}{\mathcal{R}_C + \frac{\mathcal{R}_L}{M-1}}$$

$$= \frac{Ni_1}{M\mathcal{R}_C + \mathcal{R}_L}.$$
(46)

Taking the derivative of equations (45) and (46), we find the magnetizing and leakage inductances in terms of reluctances:

$$\frac{d\Phi_1}{dt} = \frac{v_1}{N} = \frac{di_1}{dt} \frac{N(M-1)\mathcal{R}_C}{\mathcal{R}_L(M\mathcal{R}_C + \mathcal{R}_L)} = \frac{L_\mu}{N} \frac{di_1}{dt}$$

$$\rightarrow L_\mu = \frac{N^2(M-1)\mathcal{R}_C}{\mathcal{R}_L(M\mathcal{R}_C + \mathcal{R}_L)}, \tag{47}$$

and

$$\frac{d\Phi_2}{dt} = \frac{v_1}{N} = \frac{di_1}{dt} \frac{N}{M\mathcal{R}_C + \mathcal{R}_L} = \frac{L_l}{N} \frac{di_1}{dt}$$

$$\rightarrow L_l = \frac{N^2}{M\mathcal{R}_C + \mathcal{R}_L}.$$
(48)

As discussed in Section III-E, in a symmetric multiphase coupled inductor buck converter design, L_l determines the common-mode dynamics of the system, and L_μ determines the differential-mode dynamics of the system.

APPENDIX II

DERIVATION OF A STATE-SPACE MODEL OF THE MULTIPHASE COUPLED INDUCTOR BUCK CONVERTER

Equation (1) yields the dynamic equation of each phase current. For example, the equation for the current of phase 1 is:

$$N^{2} \frac{di_{1}}{dt} = (\mathcal{R}_{L} + \mathcal{R}_{C})v_{1} + \mathcal{R}_{C}v_{2} + \dots + \mathcal{R}_{C}v_{M}$$
$$= (\mathcal{R}_{L} + \mathcal{R}_{C})v_{1} + \mathcal{R}_{C} \sum_{j=2}^{j=M} v_{j}.$$
(49)

When a phase k is connected to the input voltage, $v_k = V_{IN} - i_k R_w - v_o$. When it is connected to ground, $v_k = -i_k R_w - v_o$. Only the V_{IN} term changes depending on the phase connection to input or ground; the terms relating to the internal system states are constant. Therefore, we can write a zero-input dynamic equation with no switching dependence, that is, no time dependence and no requirement for state-space averaging; then, we can superimpose the zero-input equation with the time averaged effect of the inputs using the procedure introduced in [46]. The zero-input dynamic equation with all phases grounded is

$$N^{2} \frac{di_{1}}{dt} \Big|_{\text{zero-input}} = (\mathcal{R}_{L} + \mathcal{R}_{C})(-i_{1}R_{w} - v_{o}) + \mathcal{R}_{C} \sum_{i=2}^{j=M} (-i_{j}R_{w} - v_{o}).$$

$$(50)$$

Next, we must replace v_o with an expression for the capacitor voltage:

$$v_{o} = v_{c} + R_{c} \left(\sum_{j=1}^{j=M} i_{j} - \frac{v_{o}}{R_{o}} \right)$$

$$= \frac{R_{o}}{R_{o} + R_{c}} v_{c} + (R_{c} || R_{o}) \sum_{j=1}^{j=M} i_{j},$$
(51)

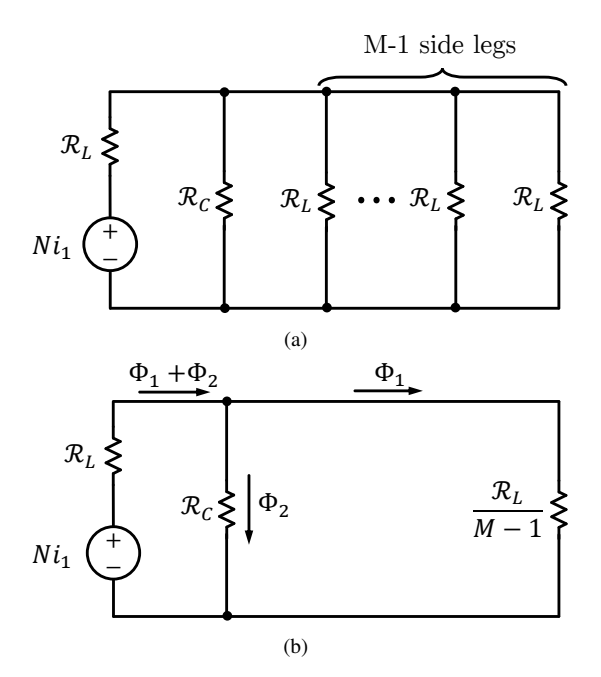


Fig. 21. (a) Reluctance model of the coupled inductor for determining leakage and magnetizing inductance of one phase with other phases open circuited. (b) Simplification of equivalent reluctances and separation of fluxes into leakage flux Φ_2 and magnetizing flux Φ_1 .

where $(R_c||R_o)$ is the parallel combination of the capacitor series resistance R_c and output resistance R_o . Substituting (51) into (50), the zero-input dynamic equation of phase 1 written in terms of internal states is:

$$N^{2} \frac{di_{1}}{dt} \Big|_{\text{zero-input}} = v_{c} \left[-(\mathcal{R}_{L} + M\mathcal{R}_{C}) \frac{R_{o}}{R_{c} + R_{o}} \right]$$

$$+ i_{1} \left[-R_{w} (\mathcal{R}_{L} + \mathcal{R}_{C}) - (R_{c} || R_{o}) (M\mathcal{R}_{C} + \mathcal{R}_{L}) \right]$$

$$+ \sum_{j=2}^{j=M} i_{j} \left[-\mathcal{R}_{C} R_{w} - (R_{c} || R_{o}) (M\mathcal{R}_{C} + \mathcal{R}_{L}) \right].$$
(52)

Equation (52) can be extended to a general zero-input dynamic equation for any phase $k=1,2,\ldots,M$.

$$\left. \frac{di_k}{dt} \right|_{\text{zero-input}} = v_c \gamma + i_k \alpha + \sum_{\substack{j=1\\j \neq k}}^{j=M} i_j \beta$$
 (53)

where

$$\alpha = \frac{-R_w(\mathcal{R}_L + \mathcal{R}_C) - (R_c||R_o)(M\mathcal{R}_C + \mathcal{R}_L)}{N^2}, \quad (54)$$

$$\beta = \frac{-\mathcal{R}_C R_w - (R_c||R_o)(M\mathcal{R}_C + \mathcal{R}_L)}{N^2},\tag{55}$$

$$\gamma = \frac{-(M\mathcal{R}_C + \mathcal{R}_L)R_o}{N^2(R_c + R_o)}.$$
 (56)

Each phase k is connected to V_{IN} for a duration d_kT during every switching period. The time averaged input contribution is therefore d_kV_{IN} for every phase. Multiplying these input contributions by their respective coefficients from (1) and superimposing with the zero-input dynamic equation (53), we find the state-space averaged dynamic equation:

$$\frac{di_k}{dt}\Big|_{\text{average}} = v_c \gamma + i_k \alpha + \sum_{\substack{j=1\\j \neq k}}^{j=M} i_j \beta + \frac{V_{IN}}{N^2} \left[(\mathcal{R}_C + \mathcal{R}_L) d_k + \mathcal{R}_C \sum_{\substack{j=1\\j \neq k}}^{j=M} d_j \right].$$
(57)

The capacitor voltage equation is obtained from the capacitor discharge through the output resistance and capacitor series resistance superimposed with the total output current being split between the series resistance and output resistance:

$$\frac{dv_c}{dt} = \frac{1}{C} \left(-\frac{v_c}{Ro + Rc} + \frac{R_o}{Ro + Rc} \sum_{j=1}^{j=M} i_j \right). \tag{58}$$

Similarly, we define the constants δ and ρ to simplify this expression:

$$\delta = \frac{R_o}{C(Ro + Rc)},\tag{59}$$

$$\rho = -\frac{1}{C(Ro + Rc)}. (60)$$

From the equations (57), (58), and the constants α , β , γ , δ , ρ , we can directly write the state-space matrices in section III-A.

APPENDIX III

SIMILARITY TRANSFORM OF THE PHASE CURRENTS

Here, we show the vectors $\mathbf{p_1}$ and $\mathbf{p_j}$ given in section III-D are eigenvectors of \mathbf{P} and find their associated eigenvalues. First, we consider the eigenvalue equation satisfied by $\mathbf{p_1}$, $\mathbf{Pp_1} = \lambda_1 \mathbf{p_1}$:

$$\begin{bmatrix} \alpha + (M-1)\beta \\ \alpha + (M-1)\beta \\ \vdots \\ \alpha + (M-1)\beta \end{bmatrix} = \lambda_1 \begin{bmatrix} 1 \\ 1 \\ \vdots \\ 1 \end{bmatrix}. \tag{61}$$

Therefore, $\mathbf{p_1}$ is an eigenvector of \mathbf{P} with associated eigenvalue $\lambda_1 = \alpha + (M-1)\beta$.

For any j = 2 ... M, $\mathbf{p_j}$ satisfies the eigenvalue equation $\mathbf{Pp_j} = \lambda_1 \mathbf{p_j}$:

$$\begin{bmatrix} \alpha - \beta \\ \vdots \\ 0 \\ \beta - \alpha \\ 0 \\ \vdots \end{bmatrix} = \lambda_{j} \begin{bmatrix} 1 \\ \vdots \\ 0 \\ -1 \\ 0 \\ \vdots \end{bmatrix}$$
 row j . (62)

Therefore, $\mathbf{p_j}$ is an eigenvector of \mathbf{P} with repeated eigenvalue $\lambda_j = \alpha - \beta$ for $j = 2 \dots M$.

Since we defined V as a matrix of the eigenvectors, we can use it to diagonalize P:

$$\mathbf{\Lambda}_{\mathbf{P}} \coloneqq \mathbf{V}\mathbf{P}\mathbf{V}^{-1} = \begin{bmatrix} \lambda_1 & 0 & \cdots & 0 \\ 0 & \lambda_2 & \cdots & 0 \\ \vdots & \vdots & \ddots & \vdots \\ 0 & 0 & \cdots & \lambda_M \end{bmatrix}. \tag{63}$$

Since the upper M by M submatrix of \mathbf{B} has the same structure as \mathbf{P} , it may be diagonalized with the same matrix of eigenvectors \mathbf{V} :

$$\mathbf{\Lambda_{R}} \coloneqq \mathbf{VRV^{-1}} = \frac{V_{IN}}{N^2} \begin{bmatrix} M\mathcal{R}_C + \mathcal{R}_L & 0 & \cdots & 0 \\ 0 & \mathcal{R}_L & \cdots & 0 \\ \vdots & \vdots & \ddots & \vdots \\ 0 & 0 & \cdots & \mathcal{R}_L \end{bmatrix}.$$
(64)

Here, the eigenvalues on the diagonals of $\Lambda_{\mathbf{R}}$ have been found by substituting the appropriate elements of \mathbf{R} in the expressions for λ_1 and λ_j .

To obtain the transformed state equation (32), we derive the expression for \mathbf{TAT}^{-1}

$$\mathbf{TAT^{-1}} = \begin{bmatrix} \mathbf{V} & \mathbf{0}_{M \times 1} \\ \mathbf{0}_{1 \times M} & 1 \end{bmatrix} \begin{bmatrix} \mathbf{P} & \mathbf{\gamma}_{M \times 1} \\ \mathbf{\delta}_{1 \times M} & \rho \end{bmatrix} \begin{bmatrix} \mathbf{V}^{-1} & \mathbf{0}_{M \times 1} \\ \mathbf{0}_{1 \times M} & 1 \end{bmatrix}$$

$$= \begin{bmatrix} \mathbf{VPV^{-1}} & \mathbf{V}_{M \times 1} \\ \mathbf{\delta}_{1 \times M} & \rho \end{bmatrix}$$

$$= \begin{bmatrix} \mathbf{\Lambda}_{\mathbf{P}} & M \mathbf{\gamma} \\ \mathbf{\delta} & \mathbf{0}_{1 \times M - 1} & \rho \end{bmatrix}.$$

$$(65)$$

where $\gamma_{M\times 1}$ and $\delta_{1\times M}$ are blocks of all γ or δ elements, as seen in the original **A** matrix formulation in (6). We have also substituted the relations (63) and (64). $\mathbf{V}\gamma_{M\times 1}$ is computed by inspection, as all elements cancel except in the first row. $\delta_{1\times M}\mathbf{V}^{-1}$ is computed by recognizing that $\delta_{1\times M}$ is proportional to the first row of \mathbf{V} and that $\mathbf{V}\mathbf{V}^{-1} = \mathbf{I}$:

$$\boldsymbol{\delta}_{1\times M}\mathbf{V^{-1}} = \delta(\mathbf{V})_{\text{row }1}\mathbf{V^{-1}} = \delta(\mathbf{V}\mathbf{V^{-1}})_{\text{row }1} \begin{bmatrix} \delta & 0_{1\times M-1} \end{bmatrix}.$$
(66)

The expression for TBV^{-1} is

$$\mathbf{TBV^{-1}} = \begin{bmatrix} \mathbf{V} & \mathbf{0}_{1 \times M} & \mathbf{0}_{M \times 1} \\ \mathbf{0}_{1 \times M} & \mathbf{1} \end{bmatrix} \begin{bmatrix} \mathbf{0}_{M \times 1} \\ \mathbf{0}_{1 \times M} \end{bmatrix} \mathbf{V^{-1}}$$

$$= \begin{bmatrix} \mathbf{VRV^{-1}} \\ \mathbf{0}_{1 \times M} \end{bmatrix}$$

$$= \begin{bmatrix} \mathbf{\Lambda_{R}} \\ \mathbf{0}_{1 \times M} \end{bmatrix}.$$
(67)

APPENDIX IV

AMPLITUDE OF CURRENT IMBALANCE CAUSED BY INPUT VOLTAGE STEP

Figure 22 illustrates an input voltage step for a four-phase system occurring between phase 1 and phase 2 being connected to the input voltage with $d < \frac{1}{4}$. Phase currents 3 and 4 are not shown. Since $V_{IN,NEW}$ is lower than $V_{IN,OLD}$ as drawn, i_2 ramps up less than it normally would in steady state. For this discussion, we take the current imbalance caused by the voltage step as i_1-i_2 at the time phase 2 is disconnected from $V_{IN,NEW}$, that is, at $t=\frac{T}{M}+dT$ in an M-phase system. After this time, phase 1 and phase 2 see the same input voltage and current balancing occurs.

To find the current imbalance $(i_1 - i_2)|_{t = \frac{T}{M} + dT}$ resulting from this input voltage step, we must compute Δi_a , Δi_b , Δi_c , and Δi_d as shown in Fig. 22. $\Delta i_a + \Delta i_b$ is the current imbalance at the start of phase 2, where phase current 2 is

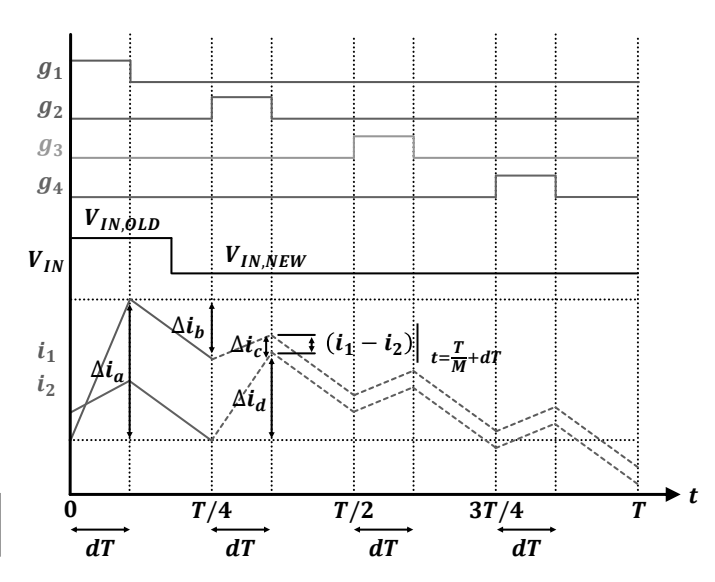


Fig. 22. Input voltage step occurring between two phases being driven causing a transient current imbalance. The dotted lines show the currents after they deviate from their original levels due to the new input voltage $V_{IN,NEW}$.

at a minimum. Δi_b is negative as drawn in Fig. 22. Δi_c and Δi_d are the increases in phase currents i_1 and i_2 respectively during driving phase 2. $\Delta i_a + \Delta i_b + \Delta i_c - \Delta i_d$ is the current imbalance caused by the step. To simplify our analysis, we assume the winding resistance R_w is zero and the output voltage is constant while the imbalance is being generated. From equation (1), we can find Δi_a as

$$\Delta i_a = \frac{dT}{N^2} [(\mathcal{R}_C + \mathcal{R}_L)v_1 + \mathcal{R}_C(v_2 + v_3 + \dots + v_M)], (68)$$

where $v_1 = V_{IN,OLD} - v_o$, $v_2 = v_3 = \cdots = v_M = -v_o$, and $v_o = dV_{IN,OLD}$. The output voltage is at steady state based on the constant duty cycle d and old output voltage. Δi_b may be found similarly to (68) as

$$\Delta i_b = \frac{\frac{T}{M} - dT}{N^2} [(\mathcal{R}_C + \mathcal{R}_L) v_1 + \mathcal{R}_C (v_2 + v_3 + \dots + v_M)], (69)$$

where $v_1 = v_2 = \cdots = v_4 = -v_o$. The current ramps Δi_c and Δi_d occur after the input voltage step. They can be found like equation (68) as well:

$$\Delta i_c = \frac{dT}{N^2} [(\mathcal{R}_C + \mathcal{R}_L) v_1 + \mathcal{R}_C (v_2 + v_3 + \dots + v_M)], (70)$$

$$\Delta i_d = \frac{dT}{N^2} [(\mathcal{R}_C + \mathcal{R}_L) v_2 + \mathcal{R}_C (v_1 + v_3 + \dots + v_M)], (71)$$

where $v_2 = V_{IN,NEW} - v_o$ and $v_1 = v_3 = v_4 = -v_o$. The output voltage is still $v_o = dV_{IN,OLD}$, as it does not change instantaneously with the input voltage. Combining all the current ramps, the differential current generated by the voltage step is

$$(i_1 - i_2)|_{t = \frac{T}{M} + dT} = \Delta i_a + \Delta i_b + \Delta i_c - \Delta i_d$$

$$= \frac{dT\mathcal{R}_L}{M} [(M - 1)V_{IN,OLD} - MV_{IN,NEW}].$$
(72)

For constant a input voltage $V_{IN,OLD} = V_{IN,NEW}$, equation (72) indicates there is still a nonzero current imbalance. This is correct, as phase 1 and 2 are interleaved and i_1 and

 i_2 are not equal at $t=\frac{T}{M}+dt$. As equation (72) suggests, the current imbalance if the input voltage was constant at $V_{IN,NEW}$ would be $-\frac{dT\mathcal{R}_LV_{IN,NEW}}{M}$. This is the normal imbalance existing due to interleaving and the value that any additional current imbalance will settle towards. Since we are interested in the additional imbalance caused by the input voltage step, we subtract the imbalance due to interleaving and obtain

$$\Delta(i_1 - i_2) := \frac{dT\mathcal{R}_L(M-1)}{M} (V_{IN,OLD} - V_{IN,NEW}), (73)$$

the additional current imbalance caused by an input voltage step. This imbalance decays to zero due to the current balancing mechanism.

REFERENCES

- [1] D. Zhou, Y. Elasser, J. Baek, C. R. Sullivan and M. Chen, "Inductance Dual Model and Control of Multiphase Coupled Inductor Buck Converter," *IEEE Workshop on Control and Modeling for Power Electronics* (COMPEL), Aalborg, Denmark, 2020, pp. 1-8.
- [2] X. Zhou, P.-L. Wong, P. Xu, F. C. Lee, and A. Q. Huang, "Investigation of Candidate VRM Topologies for Future Microprocessors," *IEEE Transactions on Power Electronics*, vol. 15, no. 6, pp. 1172-1182, Nov. 2000.
- [3] M. Chen and C. R. Sullivan, "Unified Models for Coupled Inductors Applied to Multiphase PWM Converters," *IEEE Transactions on Power Electronics*, accepted.
- [4] C. R. Sullivan and M. Chen, "Coupled Inductors for Fast-Response High-Density Power Delivery: Discrete and Integrated," *IEEE Custom Integrated Circuits Conference (CICC)*, 2021, pp. 1-8.
- [5] Y. Dong, "Investigation of Multiphase Coupled-Inductor Buck Converters in Point-of-Load Applications," *PhD Thesis*, Virginia Tech, Blacksburg, VA. Mar., 2009.
- [6] P.-L. Wong, P. Xu, P. Yang, and F.C. Lee, "Performance Improvements of Interleaving VRMs with Coupling Inductors," *IEEE Transactions on Power Electronics*, vol. 16, no. 4, pp. 499–507, 2001.
- [7] J. Li, C. R. Sullivan, A. Schultz, "Coupled Inductor Design Optimization for Fast-response Low-Voltage DC-DC Converters," *IEEE Applied Power Electronics Conference and Exposition (APEC)*, 2002, pp. 817–823 vol.2.
- [8] J. Li, A. Stratakos, C. R. Sullivan, A. Schultz, "Using Coupled Inductors to Enhance Transient Performance of Multi-Phase Buck Converters," *IEEE Applied Power Electronics Conference and Exposition (APEC)*, 2004, pp. 1289–1293 vol.2.
- [9] A. V. Ledenev, G. G. Gurov, and R. M. Porter, "Multiple Power Converter System Using Combining Transformers", US Patent US 6,545,450 B1, April 8, 2003.
- [10] B. Miwa, "Interleaved Conversion Techniques for High Density Power Supplies," *PhD Thesis*, Massachusetts Institute of Technology, 1992.
- [11] C. Chang and M. A. Knights, "Interleaving Technique in Distributed Power Conversion Systems," *IEEE Transactions on Circuits and Systems I: Fundamental Theory and Applications*, vol. 42, no. 5, pp. 245-251, May 1995.
- [12] D. O. Boillat and J. W. Kolar, "Modeling and Experimental Analysis of a Coupling Inductor Employed in a High Performance AC Power Source," *International Conference on Renewable Energy Research and Applications (ICRERA)*, Nagasaki, 2012, pp. 1-18.
- [13] D. J. Perreault and J. G. Kassakian, "Effects of Firing Angle Imbalance on 12-pulse Rectifiers with Interphase Transformers," *IEEE Transactions* on Power Electronics, vol. 10, no. 3, pp. 257-262, May 1995.
- [14] P. Zumel, O. Garcia, J. A. Cobos, J. Uceda, "Magnetic Integration for Interleaved Converters," *IEEE Applied Power Electronics Conference* (APEC), APEC03.
- [15] A. M. Schultz and C. R. Sullivan, "Voltage Converter with Coupled Inductive Windings, and Associated Methods," U.S. Patent 6,362,986, March 26, 2002.
- [16] Q. Li, Y. Dong, F. C. Lee and D. J. Gilham, "High-Density Low-Profile Coupled Inductor Design for Integrated Point-of-Load Converters," *IEEE Transactions on Power Electronics*, vol. 28, no. 1, pp. 547-554, Jan. 2013.
- [17] M. Hirakawa, M. Nagano, Y. Watanabe, K. Andoh, S. Nakatomi and S. Hashino, "High Power Density DC/DC Converter using the Close-Coupled Inductors," *IEEE Energy Conversion Congress and Exposition* (ECCE), San Jose, CA, 2009, pp. 1760-1767.

- [18] B. C. Barry et al., "Small-Signal Model and Control of the Interleaved Two-Phase Coupled-Inductor Boost Converter," *IEEE Energy Conversion Congress and Exposition (ECCE)*, Milwaukee, WI, 2016, pp. 1-6.
- [19] B. C. Barry et al., "Small-Signal Model of the Two-Phase Interleaved Coupled-Inductor Boost Converter," *IEEE Transactions on Power Electronics*, vol. 33, no. 9, pp. 8052-8064, Sept. 2018.
- [20] G. Zhu and K. Wang, "Modeling and Design Considerations of Coupled Inductor Converters," *IEEE Applied Power Electronics Conference and Exposition (APEC)*, 2010.
- [21] G. Zhu, B. A. McDonald and K. Wang, "Modeling and Analysis of Coupled Inductors in Power Converters," *IEEE Transactions on Power Electronics*, vol. 26, no. 5, pp. 1355-1363, May 2011.
- [22] N. Kondrath and M. K. Kazimierczuk, "Control-to-Output and Duty Ratio-to-Inductor Current Transfer Functions of Peak Current-Mode Controlled Dc-Dc PWM Buck Converter in CCM," *IEEE International Symposium on Circuits and Systems*, Paris, 2010, pp. 2734-2737.
- [23] W. Wu, N.-C. Lee and G. Schuellein, "Multi-Phase Buck Converter Design with Two-Phase Coupled Inductors," *IEEE Applied Power Electronics Conference and Exposition (APEC)*, 2006, Dallas, TX, 2006.
- [24] P. Xu, J. Wei and F. C. Lee, "Multiphase Coupled-Buck Converter a Novel High Efficient 12 V Voltage Regulator Module," *IEEE Transactions* on Power Electronics, vol. 18, no. 1, pp. 74-82, Jan. 2003.
- [25] M. Xu, J. Zhou, K. Yao and F. C. Lee, "Small Signal Modeling of a High Bandwidth Voltage Regulator Using Coupled Inductors," *IEEE Transactions on Power Electronics*, vol. 22, no. 2, pp. 399-406, March 2007.
- [26] Y. Qiu, M. Xu, K. Yao, J. Sun and F. C. Lee, "Multifrequency Small-Signal Model for Buck and Multiphase Buck Converters," *IEEE Transactions on Power Electronics*, vol. 21, no. 5, pp. 1185-1192, Sept. 2006.
- [27] X. Sun, Y.-S. Lee and D. Xu, "Modeling, Analysis, and Implementation of Parallel Multi-Inverter Systems with Instantaneous Average-Current-Sharing Scheme," *IEEE Transactions on Power Electronics*, vol. 18, no. 3, pp. 844-856, May 2003.
- [28] Y. Panov and M. M. Jovanovic, "Stability and Dynamic Performance of Current-Sharing Control for Paralleled Voltage Regulator Modules," *IEEE Applied Power Electronics Conference and Exposition (APEC)*, Anaheim, CA, USA, 2001, pp. 765-771.
- [29] X. Zhou, P. Xu and F. C. Lee, "A Novel Current-Sharing Control Technique for Low-Voltage High-Current Voltage Regulator Module Applications," *IEEE Transactions on Power Electronics*, vol. 15, no. 6, pp. 1153-1162, Nov. 2000.
- [30] M. Tsai, D. Chen, C. Chen, C. Chiu and W. Chang, "Modeling and Design of Current Balancing Control in Voltage-Mode Multiphase Interleaved Voltage Regulators," *International Power Electronics Conference* (IPEC), Sapporo, 2010.
- [31] C. -J. Chen, Z. -Y. Zeng, C. -H. Cheng and F. -T. Lin, "Comprehensive Analysis and Design of Current-Balance Loop in Constant On-Time Controlled Multi-Phase Buck Converter," *IEEE Access*, vol. 8, pp. 184752-184764, 2020
- [32] D. Jovanović, H. Pezeshki, M. A. H. Broadmeadow, G. R. Walker and G. F. Ledwich, "Current-Balancing Technique for Paralleled Interleaved Inverters with Magnetically Coupled Inductors," *IEEE International Con*ference on Power Electronics and Drive Systems (PEDS), Honolulu, HI, 2017.
- [33] D. P. Jovanović, M. A. H. Broadmeadow, R. R. Taylor, G. R. Walker and G. F. Ledwich, "Decoupling of Current Balancing and Reference Tracking Control in Parallel Interleaved Converters," *IEEE Transactions* on *Power Electronics*, vol. 35, no. 4, pp. 4286-4295, April 2020.
- [34] S. Utz and J. Pforr, "Impact of Input and Output Voltage Perturbation on the Behavior of Automotive Multi-Phase Converters with Coupled Inductors," *IEEE Energy Conversion Congress and Exposition*, Phoenix, AZ, 2011, pp. 4169-4176.
- [35] F. J. B. Brito, M. L. Heldwein and R. P. T. Bascopé, "Active Current Balancing Technique Employing the Lunze's Transformation for converters based on Multistate Switching Cells," *IEEE Brazilian Power Electronics Conference and Southern Power Electronics Conference (COBEP/SPEC)*, Fortaleza, 2015, pp. 1-6.
- [36] B. Oraw and R. Ayyanar, "Stability of Multi-Winding Coupled Inductors in Buck Converters," *IEEE International Telecommunications Energy Conference (INTELEC)*, San Diego, CA, 2008, pp. 1-6.
- [37] M. Le Bolloch, M. Cousineau and T. Meynard, "Current-Sharing Control Technique for Interleaving VRMs using Intercell Transformers," European Conference on Power Electronics and Applications, Barcelona, 2009, pp. 1-10.
- [38] C. Gautier, F. Adam, E. Laboure, B. Revol and D. Labrousse, "Control for the Currents Balancing of a Multicell Interleaved Converter with ICT,"

- European Conference on Power Electronics and Applications (EPE), Lille, 2013, pp. 1-9.
- [39] C. Garreau and G. Gateau, "Modeling and Generalization of Parallel Multilevel Converter for the Design of the Closed Loop's Controllers," *IEEE International Conference on Industrial Technology (ICIT)*, Toronto, ON, 2017, pp. 153-158.
- [40] H. N. Nagaraja, D. Kastha and A. Petra, "Design Principles of a Symmetrically Coupled Inductor Structure for Multiphase Synchronous Buck Converters," *IEEE Transactions on Industrial Electronics*, vol. 58, no. 3, pp. 988-997, March 2011.
- [41] W. Hu, C. Chen, S. Duan, W. Wan, L. Song and J. Zhu, "Decoupled Average Current Balancing Method for Interleaved Buck Converters with Dual Closed-Loop Control," *IEEE 9th International Power Electronics* and Motion Control Conference (IPEMC2020-ECCE Asia), 2020, pp. 578-583
- [42] Y. Yan and E. Gu, "A Scalable Multiphase Current-Mode Buck Controller With Sub-Milliohm DCR Current Sensing and Synchronized Overcurrent Protection," *IEEE Journal of Solid-State Circuits*, 2021.
- [43] S. El-Hamamsy and E. I. Chang, "Magnetics Modeling for Computer-Aided Design of Power Electronics Circuits," *IEEE Power Electronics Specialists Conference*, Milwaukee, WI, USA, 1989, pp. 635-645 vol.2.
- [44] E. C. Cherry, "The Duality between Interlinked Electric and Magnetic Circuits and the Formation of Transformer Equivalent Circuits," *Proceedings of the Physical Society*, vol. 62 part 2, section B, no. 350 B, Feb. 1949, pp. 101-111.
- [45] W. H. Hayt and J. E. Kemmerly, "Inductance and Capacitance: Duality," Engineering Circuit Analysis, Fourth Edition, New York: McGraw-Hill Book Company, 1993.
- [46] R. D. Middlebrook and S. Cuk, "A General Unified Approach to Modelling Switching-Converter Power Stages," *IEEE Power Electronics Specialists Conference*, Cleveland, OH, 1976, pp. 18-34.
- [47] G. W. Wester and R. D. Middlebrook, "Low-Frequency Characterization of Switched dc-dc Converters," *IEEE Transactions on Aerospace and Electronic Systems*, vol. AES-9, no. 3, May 1973, pp. 376-385.
- [48] Y. Chen, D. M. Giuliano and M. Chen, "Two-Stage 48V-1V Hybrid Switched-Capacitor Point-of-Load Converter with 24V Intermediate Bus," *IEEE Workshop on Control and Modeling for Power Electronics (COM-PEL)*, Aalborg, Denmark, 2020, pp. 1-8.
- [49] Y. Elasser, J. Baek and M. Chen, "A Merged-Two-Stage LEGO-PoL Converter with Coupled Inductors for Vertical Power Delivery," *IEEE Energy Conversion Congress and Exposition (ECCE)*, Detroit, MI, 2020, pp. 916-923.
- [50] Ferroxcube, "3F4 Material Specification," 3F4 datasheet, Sept 1, 2008.



Youssef Elasser (Student Member, IEEE) received the B.S. degree in electrical engineering and computer science with a concentration in electric power in 2018 from Rensselaer Polytechnic Institute, Troy, NY. He joined Princeton University, Princeton, NJ in 2018, where he is currently working towards his Ph.D. degree. His research interests include renewable energy storage systems, dc-dc power conversion, and novel magnetics design for switching power supplies. While at Rensselaer, he was the recipient of the Grainger Scholars Award for dis-

tinguished undergraduates studying electric power. At Princeton, he received the first place award from the 2019 Princeton Innovation Forum and was a recipient of the prestigious NSF Graduate Research Fellowship.



Jaeil Baek (Member, IEEE) received the B.S. degree in electronics and electrical engineering from Sungkyunkwan University, Suwon, South Korea, in 2011, and the M.S. and Ph.D. degrees in electrical engineering from the Korea Advanced Institute of Science and Technology, Daejeon, South Korea, in 2015 and 2018, respectively.

Since 2019, he has been a Postdoctoral Research Associate with the Department of Electrical and Computer Engineering and Andlinger Center for Energy and the Environment, Princeton University,

Princeton, NJ, USA. His current research interests include point-of-load power converters, grid interface power electronics, digital control approach of converters, and advanced power electronics architecture.

Dr. Baek was the recipient of the Research Outstanding Award from the Korea Advanced Institute of Science and Technology and Global Ph.D. Fellowship and Postdoctoral Fellowship from the National Research Foundation of Korea.



Daniel H. Zhou (Student Member, IEEE) received the B.A.Sc degree in mechatronics engineering from the University of Waterloo, Waterloo, Canada, in 2019. He received the M.A. degree in electrical engineering from Princeton University, Princeton, NJ, USA in 2021 and is currently working towards the Ph.D. degree.

His research interests include ultrafast point-ofload power converters, dynamic modeling and control of power electronics, and power magnetics design.

Mr. Zhou was the recipient of the Colonel Hugh Heasley Engineering Scholarship at the University of Waterloo. At Princeton University, he was awarded the prestigious NSERC Alexander Graham Bell Graduate Scholarship.



Minjie Chen (Senior Member, IEEE) received the B.S. degree from Tsinghua University, Beijing, China, in 2009, and the S.M., E.E., and Ph.D. degrees from Massachusetts Institute of Technology (MIT), Cambridge, MA, USA, in 2012, 2014, and 2015, respectively. He is an Assistant Professor of Electrical and Computer Engineering and Andlinger Center for Energy and the Environment at Princeton University, where he leads the Princeton Power Electronics Research Lab. His research interests include complex power architecture, power magnetics, con-

trol, and machine learning methods for high performance power electronics.

Dr. Chen is the Vice Chair of IEEE PELS Technical Committee on Design Methodologies (TC10), Associate Editor of IEEE Transactions on Power Electronics, Associate Editor of IEEE Journal of Emerging and Selected Topics in Power Electronics, Associate Technical Program Committee Chair of IEEE Energy Conversion Congress and Exposition (ECCE) in 2019, Student Activity Chair of IEEE Energy Conversion Congress and Exposition (ECCE) in 2020, and the Technical Program Committee Chair of IEEE International Conference on DC Microgrids (ICDCM) in 2021.

Dr. Chen received three IEEE Transactions Prize Paper Awards (2016, 2017, 2020), a COMPEL Best Paper Award (2020), the NSF CAREER Award, a Dimitris N. Chorafas Award for outstanding MIT Ph.D. Thesis, an Outstanding Reviewer Award from IEEE Transactions on Power Electronics, two ECCE Best Demonstration Awards, multiple APEC Outstanding Presentation Awards, a Siebel Energy Institute Research Award, a C3.ai DTI Research Award, and the First Place Award from the Innovation Forum of Princeton University. He was included in the Princeton Engineering Commendation List for Outstanding Teaching. He holds 6 U.S. patents.